Final Report

DOE-Project: DE-SC0002391

Charging and Heating Dynamics of Nanoparticles in Nonthermal Plasmas

University of Minnesota-Twin Cities

Project Personnel:

Principal Investigator: Dr. Uwe Kortshagen, Professor, Mechanical Engineering

Graduate Research Assistants:

Dr. Federico Galli	former Ph.D. Student, Mechanical Engineering
Dr. Meenakshi Manunuru	former Ph.D. Student, Mechanical Engineering
Nicolaas Kramer	Ph.D. Student, Mechanical Engineering

August 15, 2014

Executive Summary

The focus of this award was to understand the interactions of nanometer-sized particles with ionized gases, also called plasmas. Plasmas are widely used in the fabrication of electronic circuits such as microprocessors and memory devices, in plasma display panels, as well as in medical applications. Recently, these ionized gases are finding applications in the synthesis of advanced nanomaterials with novel properties, which are based on nanometer-sized particulate (nanoparticles) building blocks. As these nanoparticles grow in the plasma environment, they interact with the plasmas species such as electrons and ions which critically determines the nanoparticle properties.

The University of Minnesota researchers conducting this project performed numerical simulations and developed analytical models that described the interaction of plasma-bound nanoparticles with the plasma ions. The plasma ions bombard the nanoparticle surface with substantial energy, which can result in the rearrangement of the nanoparticles' atoms, giving them often desirable structures at the atomic scale. Being able to tune the ion energies allows to control the properties of nanoparticles produced in order to tailor their attributes for certain applications. For instance, when used in high efficiency light emitting devices, nanoparticles produced under high fluxes of highly energetic ions may show superior light emission to particles produced under low fluxes of less energetic ions.

The analytical models developed by the University of Minnesota researchers enable the research community to easily determine the energy of ions bombarding the nanoparticles. The researchers extensively tested the validity of the analytical models by comparing them to sophisticated computer simulations based on stochastic particle modeling, also called Monte Carlo modeling, which simulated the motion of hundreds of thousands of ions and their interaction with the nanoparticle surfaces.

Beyond the scientific intellectual merits, this award had significant broader impacts. Two graduate students received their doctoral degrees and both have joined a U.S. manufacturer of plasma-based semiconductor processing equipment. Four undergraduate

students participated in research conducted under this grant and gained valuable hands-on laboratory experience. A middle school science teacher observed research conducted under this grant and developed three new course modules that introduce middle school students to the concepts of nanometer scale, the atomic structure of matter, and the composition of matter of different chemical elements.

Activities

The objective of this grant was to explore the interactions on nanoparticles with nonthermal plasmas through theory, modeling, and experiments. This grant provides partial funding for a project that was co-funded by DOE grant DE-SC0002391.

Under this grant, we mainly focused on the modeling of nanoparticle charging and of the ion energy distribution of ions hitting the nanoparticles. In this study, we developed a self-consistent particle in cell/Monte Carlo collision (PIC/MCC) simulation for the ions in the sheath around the nanoparticles. The simulation was similar to the one developed by Gatti and Kortshagen [1]. The problem was simplified by assuming spherical symmetry around the particle, making the simulation one-dimensional. The equation of motion was solved for the ions in the simulation domain. Collisions of ions with neutrals were treated with a Monte Carlo approach. Electrons were described with a continuum approach. The electric field and the potential profile around the particle was determined by integration of the Poisson equation over the instantaneous charge distribution.

The simulation domain extended to five linearized Debye lengths from the particle surface. The simulation domain was divided into 1000 radial cells with a slightly exponentially increasing cell size with growing distance from the particle surface. The minimum cell size was 10 nm. For a given potential profile, the ion trajectory between collisions was determined with a velocity Verlet algorithm. A continuously updated record was kept of ion positions, velocities, angular momenta and collision times. The collision times were calculated from the maximum collision frequency as a function of energy. When the simulation time matches the collision time for a given ion, a null-collision Monte Carlo method was applied to determine the nature of the collision (real or null) and a new collision time was calculated. The collisions can affect both the electric field around the particle and more significantly the energy of ions reaching the surface of the nanoparticle. As the ion motion was continuously tracked, “trapped” ions that were on a closed orbit around the particle were self-consistently accounted for in the simulation. Ions leaving the simulation domain or being absorbed by the nanoparticle

were replaced by ions entering the simulation domain, which were assumed to have a Maxwellian energy distribution in the unperturbed plasma.

Electrons have a much smaller mass and a much larger velocity. Hence, a continuum approach was adopted for the electrons. The electron fluxes to the nanoparticle were derived assuming Boltzmann distributed electrons in the case of a Maxwellian and an equivalent distribution for non-Maxwellian electrons. The potential $V(r)$ and electric field $E(r)$ in the simulation domain were found from the integration of the Poisson equation. The Poisson equation was solved subject to the boundary conditions that the electric field at the particle surface was given by the particle charge Q_p and the capacitance of a sphere and that the potential at the edge of the simulation domain was zero.

As the electron density and the electric potential depend on each other, an iterative approach was adopted to find their self-consistent profiles. Since the effect of screening close to the particle was small for the nanoparticles considered here, this approach converges rapidly. At the beginning of the simulation, an initial guess of the potential profile was made based on a shielded Yukawa potential assuming an initial particle charge. The domain was then filled with ions at the prescribed density and initially at room temperature. The initial ion population was allowed to relax in the initial Yukawa potential, which was held constant during the relaxation process. The simulation then switched to a full self-consistent mode. In this mode the ions were moved for a time step dt=1 ps and the Poisson equation was solved as described above. The time step of 1 ps was short enough to accurately resolve the ion motion even close to the nanoparticle. The simulation was allowed to proceed until a steady electric potential around the nanoparticle was found.

Ions that leave the simulation cell through impacting on the particle surface contribute to the particle charge and their impaction velocities were registered. A histogram of collection frequencies against impact energy was created and updated for each charging event.

In our paper by Gatti et al [1], we also presented a novel, fully analytical model for nanoparticle charging for a single component plasma. One important aspect of this work was that the model developed was applicable over a wide range of pressures from very low pressures to atmospheric pressures. The analytical model relied on describing the ion current to a particle by three components, which, depending on the pressure range, were "turned on" or "turned off" by appropriate pressure dependent weight factors. The Orbital Motion Limited (OML) model was used to describe the collisionless plasma regime, a collision-enhanced current model described weakly collisional plasmas, and the hydrodynamic regime for fully collisional plasmas. In ref. 1, we were able to show that the simple analytical model was in excellent agreement with computationally very extensive Monte Carlo (MC)-Particle in Cell simulations.

During this project, we also extended both models, the Monte Carlo simulation and the analytical model, to include two different types of ions. This was a quite important step, since in most chemically active plasmas, multiple ion species were present. We developed a model for particles suspended in a argon:hydrogen plasma, due to its importance for many dusty plasma situations. Particle formation in argon:silane (SiH_4) plasmas has long been the prototypical dusty plasma situation, leading to silicon particles being immersed in an argon:hydrogen plasma. We began with considering a mixture of hydrogen and argon ions, Ar^+ and H_3^+ in low pressure argon gas. Particle charging was studied by parameterizing the ratio of argon and hydrogen ions. The analysis calculated the particle potential for a given effective electron temperature, pressure, ion densities, ion temperatures, and nanoparticle radius.

Broader Impact Activities

Integration of teaching, training and research: This project, and its DOE counterpart, involved two graduate students, Federico Galli and Meenakshi Mamunuru. Federico was supported for the final year of his Ph.D. thesis and has since assumed a job at Novellus as a plasma processing/modeling engineer. Meenakshi is currently finishing her Ph.D. thesis and has recently interviewed at Novellus, also as a plamas processing/modeling engineer. Both students received an excellent research training in plasma physics and plasma processing.

During this grant period, Kortshagen hosted a middle school science teacher for an RET (Research Experience for Teachers) experience. Mr. Leonardo Santiago, a science teacher at Aurora middle school in Minneapolis, MN, a primarily Hispanic serving charter school, spent six weeks in Kortshagen's lab to learn about the scientific process involved in plasma and nanoparticle research. Mr. Santiago shadowed several of Kortshagen's graduate students and developed three course modules based on his experiences. These class modules were:

1. "Appreciating the nanoscale." Introducing nanoscale through number analogies and analogies to daily life, e.g. "Imagine a traffic jam with 1000 pick-up trucks, each loaded with 1000 boxes of Legos, each box containing 1000 Legos."

2. "Element, compound, mixture." A module to give students an appreciation of elements, compounds, and mixtures using different materials such as metals, rocks and minerals, and differently colored miscible liquids to prepare solutions.

3. "Particle model of solids and gases." A module based on ball and stick atomic tool kits to identify essential properties of solids and gases.

Participation of underrepresented groups: Kortshagen is member of the Minnesota Materi- als Research Science and Engineering Center (MRSEC), which has significant efforts to enhance the participation of underrepresented minorities. He participated in the

MRSEC REU program and hosted undergraduate students in his lab for two of the three summers of this grant. Ms. Bryne Berry (from Iowa State University) worked in his lab on nanoparticle synthesis with plasmas in 2011. Mr. Ruben Renya (from the University of Texas-Pan American) worked in Kortshagen's lab to study the optical properties of plasma-produced silicon crystals. Moreover, Kortshagen employed several more undergraduate students in his laboratory on research positions, among them ME undergraduate students Ms. Lauren Cantley and Ms. Jessica Malone.

Broad dissemination of results: Since becoming department head in 2008, Kortshagen has had a reduced teaching load, which did not enable him to include some of the results of this work in graduate classes that he used to teach before becoming department head. However, Kortshagen continues to remain involved in undergraduate education and he tries to incorporate some of his research in these classes as well. Moreover, Kortshagen has made significant efforts to give a broad public an appreciation of the process and the results of his research. For the past three summers, Kortshagen has organized a one-day module for groups of ~24 high school students as part of the University of Minnesota's Exploring Careers in Science and Engineering program. As part of these activities, students conducted activities including synthesizing iron nanoparticles to produce ferrofluids, learning about electron microscopy, and visiting research laboratories.

Findings

1. Ion energy distribution functions of ions hitting nanoparticles in a single component plasma[1]

Initial studies were devoted to the impact of different kinds of electron energy distribution functions (EEDFs) and of the discharge pressure on the ion energy distribution (IED) of ions impinging on nanoparticle surfaces. Figure 1 compares IEDs for both Maxwellian and non-Maxwellian distribution functions for a 500 nm particle in an argon plasma with E/N=10 Td. The corresponding temperature of the Maxwellian EDF, defined as 2/3 the mean kinetic energy of the non-Maxwellian EDF, is 3.4 eV. Figure 1 reveals two important facts about the IEDs. First, for low pressures, the IEDs have a beam-like shape, suggesting that the ion motion in the sheath around the particle is collisionless. At the pressure of 1 Pa, a significant difference between Maxwellian and non-Maxwellian EEDFs is observed. The average energy of ions reaching the surface of the particle for a non-Maxwellian EEDF is approximately 1 eV lower than for the corresponding Maxwellian EEDF with the same effective electron temperature. At this low pressure the absolute value of the nanoparticle potential is ~7-8 V and electrons in the tail of the distribution play a significant role in the charging of the nanoparticles. As a Maxwellian EEDF contains more electrons in the energetic tail than a non-Maxwellian EEDF, a more negative nanoparticle potential is required to balance the electron flux with the ion flux. This more negative potential causes a higher ion energy in the Maxwellian EEDF case.

[1] The description of these findings has been adapted from the paper "The energy distribution function of

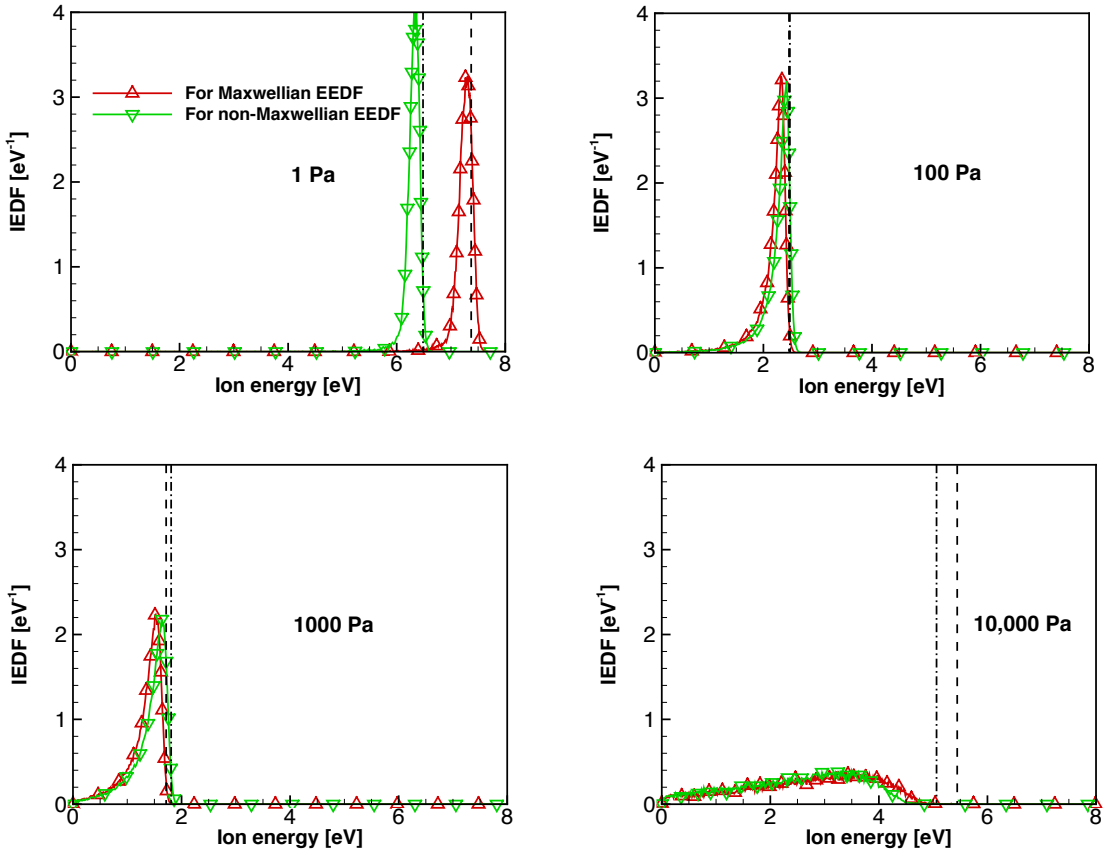

Figure 1: Results of simulations for the energy distribution of ions impacting a 500 nm particle, assuming either a Maxwellian or a non-Maxwellian electron energy distribution in argon plasma at E/N = 10 Td. n_i =1 x 10^{16} m^{-3}, pressure range p = 0.1 Pa-10,000 Pa. The effective electron temperature for both cases is 3.4 eV. The dashed line and the dot-dashed line indicate particle potentials for Maxwellian and non-Maxwellian EEDFs respectively.

The second observation is that the IEDs show a significant dependence on the discharge pressure, even though the EEDFs remain unchanged, since the effective electric field E/N and electron temperature are held constant. This behavior is a reflection of the variation of the particle floating potential with discharge pressure. The particle floating potential changes strongly, since with increasing pressure the physical regime of ion collection changes, as discussed in detail in [1]. At low pressures, the ion motion in the Debye sphere around the particle is almost collisionless and ion collection is described by the collisionless orbital motion limited theory.[2] At higher pressures, the

ion collection by the particle is enhanced by collisions of ions within the Debye sphere. In this regime, known as collision enhanced current regime, ions that would miss the particle if the motion were collisionless do get collected by the particle since their angular momentum was changed in a collision. This leads to an enhanced ion collection which causes a less negatively biased particle floating potential and thus reduced ion impact energies at the particle surface. As the particle becomes less negative, the relative importance of the EEDF tail decreases and the IEDs for the Maxwellian and non-Maxwellian EEDFs become almost identical. The IEDs also develop a low-energy tail, characteristic of ions that have undergone collisions within the sheath. As the pressure increases further, the ion motion in the particle sheath becomes strongly collisional, leading to a mobility dominated motion. In this ``hydrodynamic'' regime, the nanoparticle potential again becomes more negative, since collisions reduce the ion current to the particle. However, since the ion motion is strongly collisional, the ion energies do not proportionally follow suit.

In Figure 2 we plot the distribution of kinetic energy carried by ions impinging on the surface of a nanoparticle; we further divide the energy based on the velocity direction distinguishing between the radial velocity component and the tangential velocity component of the impinging ions. We refer to the former as ``radial energy component'' and the latter as ``tangential energy component.'' In these plots the dotted line indicates the position of the particle floating potential on the energy axis. An ion reaching a nanoparticle with high tangential component and low radial component is essentially ``grazing'' the surface of the particle, while an ion reaching with only radial component is having a collision with maximum momentum exchange. In the low pressure case, while all ions arrive with roughly the same total energy, there is a wide spread in the distributions of tangential and radial energies. As the pressure increases, the tangential energy component becomes less and less important and the ion motion becomes more and more radial as an effect of frequent collisions.

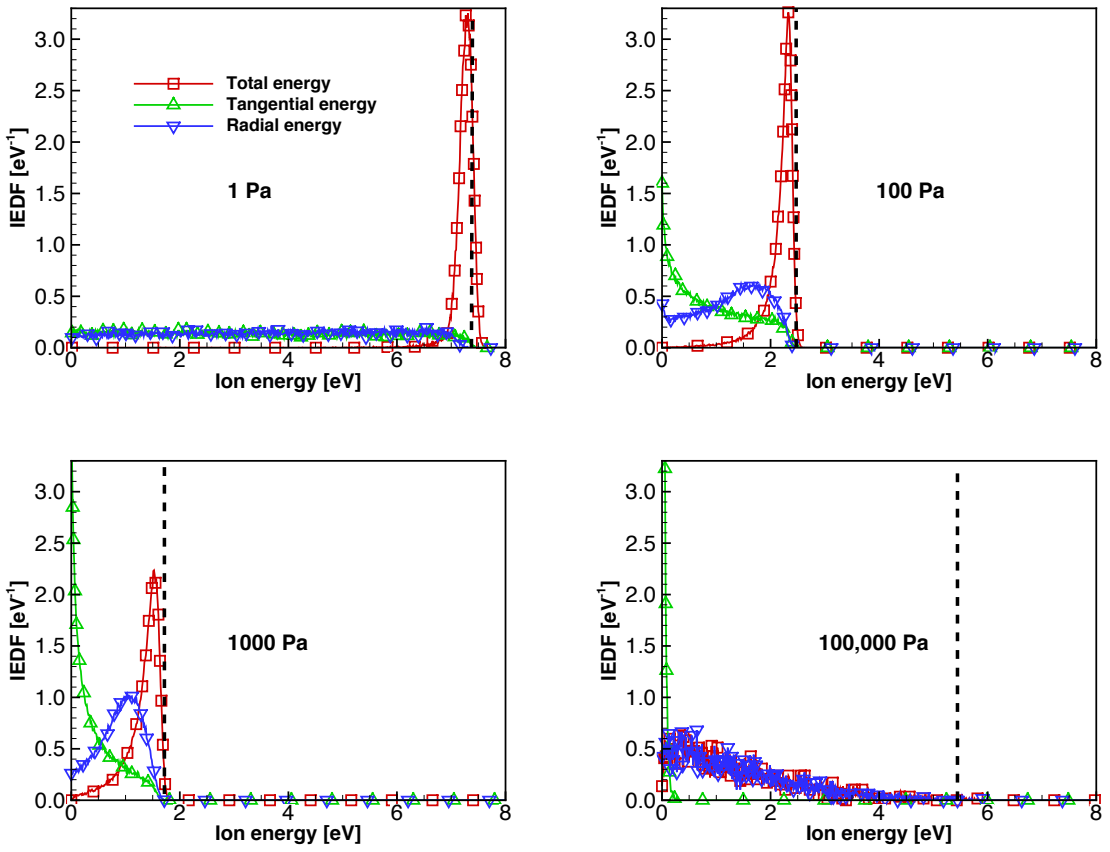

Figure 2: Results of simulations for the IED for 500 nm particles in a Maxwellian argon plasma, $n_i = 1 \times 10^{16}$ m^{-3}, $T_e = 3.4$ eV, pressure range p = 0.1 Pa - 31,600 Pa.

The effects of particle size on the IED for 500 nm particles and 50 nm particles are compared in Figure 3, respectively. For the 500 nm particle, the particle potential becomes less negative and the ion energies decrease with increasing pressure up to about 320 Pa. At higher pressures the ion current enters the hydrodynamic regime causing a more negative particle potential and an increase of the ion energies. Only at the highest pressure of 31600 Pa does the ion energy decrease again due to the highly collisional ion motion in the sheath. The 50 nm particle shows a qualitatively similar behavior, however, with a shift to higher pressures. For instance, the ion energies decrease up to a pressure of 10000 Pa. This behavior is based on the fact that a smaller particle carries a

smaller charge and is thus surrounded by a smaller Debye sphere. At the same pressure, the ion motion is more collisional in the larger sheath around the larger nanoparticle while still being less collisional in the smaller sheath around the smaller particle.

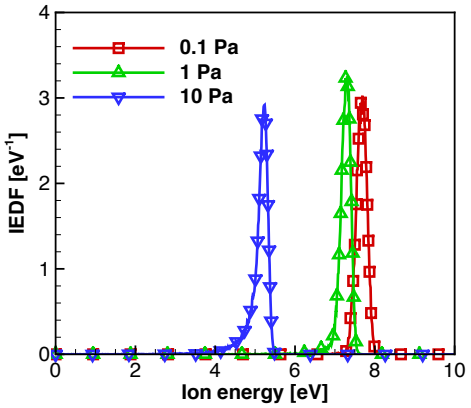
0.1 Pa
1 Pa
10 Pa
IEDF [eV^{-1}]
Ion energy [eV]

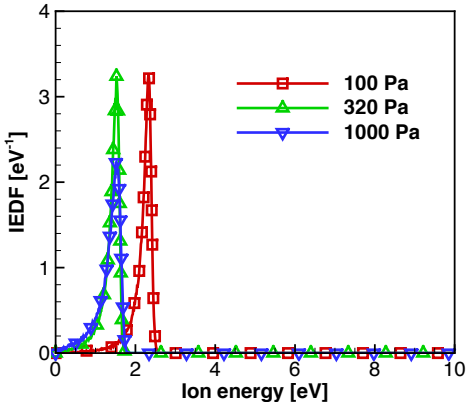
100 Pa
320 Pa
1000 Pa
IEDF [eV^{-1}]
Ion energy [eV]

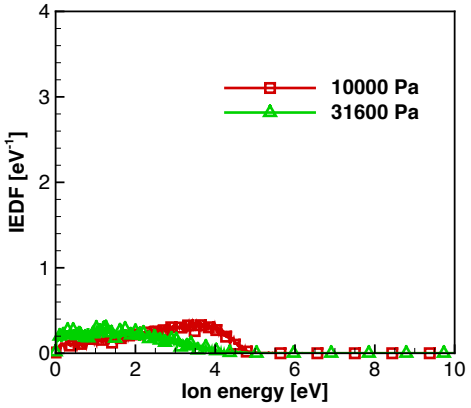
10000 Pa
31600 Pa
IEDF [eV^{-1}]
Ion energy [eV]

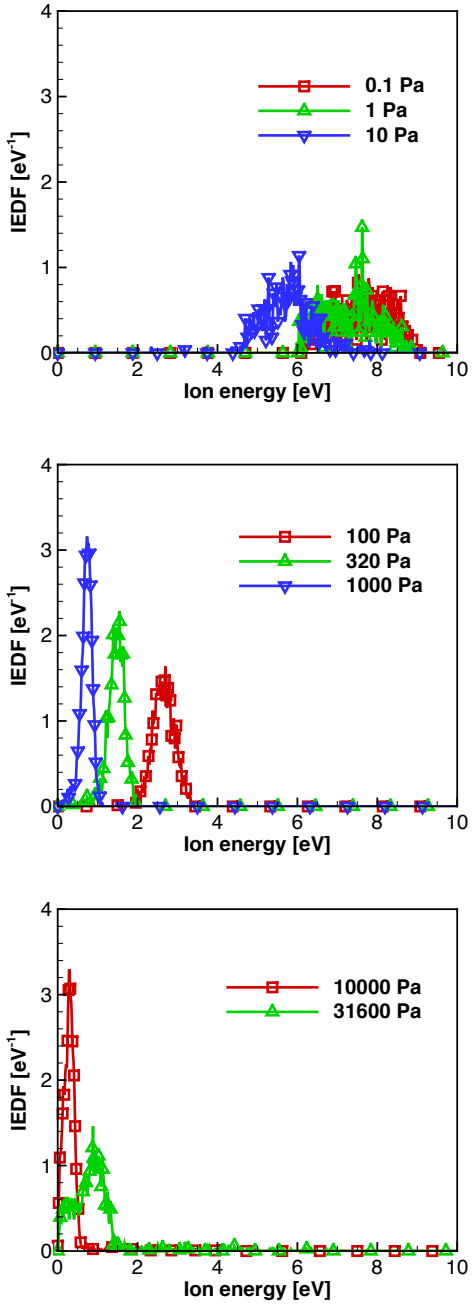

Figure 3: Results of simulations for the IED for a Maxwellian argon plasma, n_i =1 x 10^{16} m^{-3}, T_e = 3.4 eV, pressure range p = 0.1 Pa - 31,600 Pa. Left column: 500 nm particle, right column: 50 nm particle.

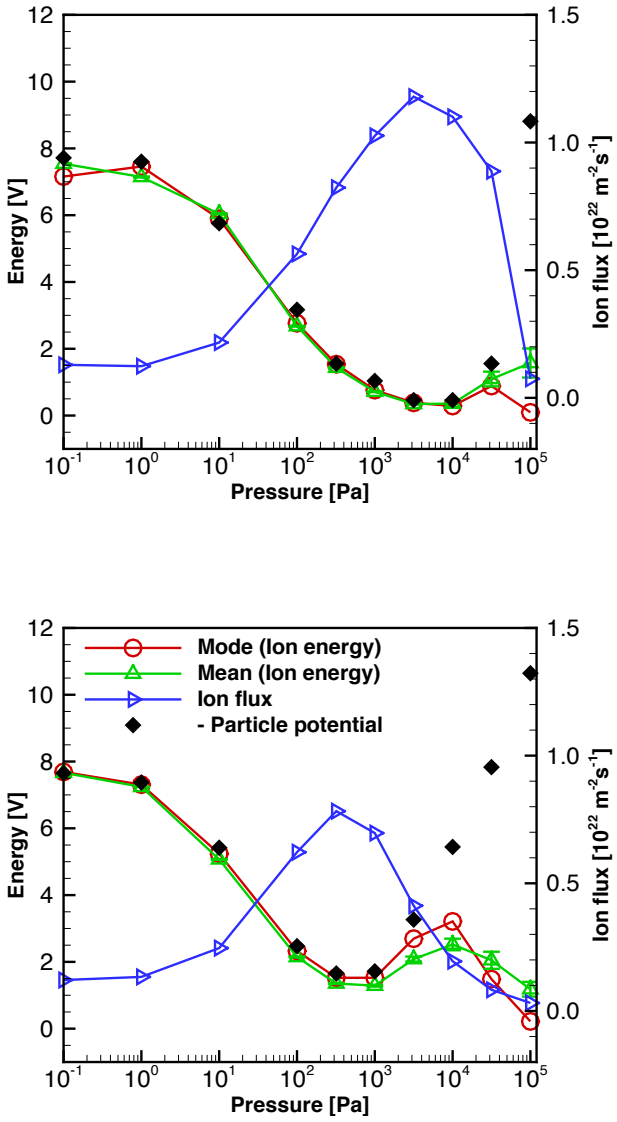

Figure 4: The absolute value of nanoparticle potential, the ion flux and the mean and mode for the energy of ions impinging on a 500 nm particle (above) and a 50 nm particle (below). Plasma parameters are as reported in Figure 3. Notice the dramatic reduction in the average ion energy and the concurrent increase in the total flux taking place in the range of pressures commonly used for the synthesis of nano-crystalline materials in low-pressure dusty plasmas.

Figure 4 summarizes the findings of Figure 3. It shows the mean and the mode for the IED as well as the predicted ion flux for the 500 nm and the 50 nm nanoparticle diameter, respectively. It is quite remarkable that in the 50 nm case the ion flux increases by almost a factor of 10 while the average ion energy drops from a value of about 7.5 eV

to a value of 0.6 eV (a 12-fold reduction). It is also worth noting that in the OML regime and in the collision enhanced regime, the mean ion energy closely follows the particle potential; however, in the hydrodynamic regime it becomes much smaller than the particle potential.

2. Ion energy distribution functions of ions hitting nanoparticles in a single component plasma[2]

We now discuss some results obtained with our analytical model. In plasma consisting of only Ar^+ ions in argon gas, the calculated particle potential is plotted in Figure 5. The particle radius is 100 nm, the ion density, $1\times10^{16}\,m^{-3}$, effective electron temperature, 3.5 eV, and the plasma is at room temperature.

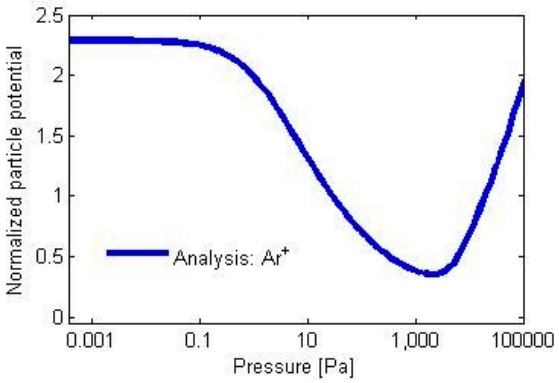

Figure 5: Normalized particle potential (= - particle potential/kTe) versus pressure for a plasma consisting of Ar^+ ions in argon.

In the low pressure range (< 0.1 Pa), the potential is described by OML theory. At pressures between 0.1 and 1000 Pa, which shall henceforth be called intermediate pressures, there is a reduction in the potential due to the collisional enhancement of the ion currty. At higher pressures the potential rises again, since increasing collisions reduce the ion current to the particle, leading to more negatively charged particles. This behavior is explained by the ion current to the particle (Figure 6). The particle potential is reduced

[2] These findings are currently being prepared for publication in and will be part of Meenakshi Mamunuru's forthcoming Ph.D. thesis. These results had previously been reported in the 2011 annual report.

by collision enhanced ion current at intermediate pressures. At even higher pressures, the ion transport becomes mobility limited and the ion flux reduces as pressure increases because it is inhibited by multiple collisions with the neutral gas. Figure 6 compares the potential in Figure 5, with the potential obtained when we replace half the Ar^+ ions in argon gas with H_3^+ ions. Thus we are comparing potentials when the total ion density is the same, but the ion constitution is different. All other parameters are kept constant. Also compared are the ion currents in both cases. Consider the low pressure regime. The total current is greater in case of the ion mixture, due to lower mass of H_3^+ resulting in a higher thermal ion current. In the intermediate pressure range, the total ion current is comparable for both cases. This is because the current in the mixture is dominated by collision enhanced Ar^+ ions. So the potential almost overlaps the pure Ar^+ ions case. However, in the high pressure regime, while the argon current is inhibited due to excessive collisions, the collision enhanced H_3^+ ion current takes over, causing the potential to continue to remain lower. The analytical model suggests that H_3^+ ion current dominates in the low and high pressure ranges, while Ar^+ current dominates in the intermediate pressures.

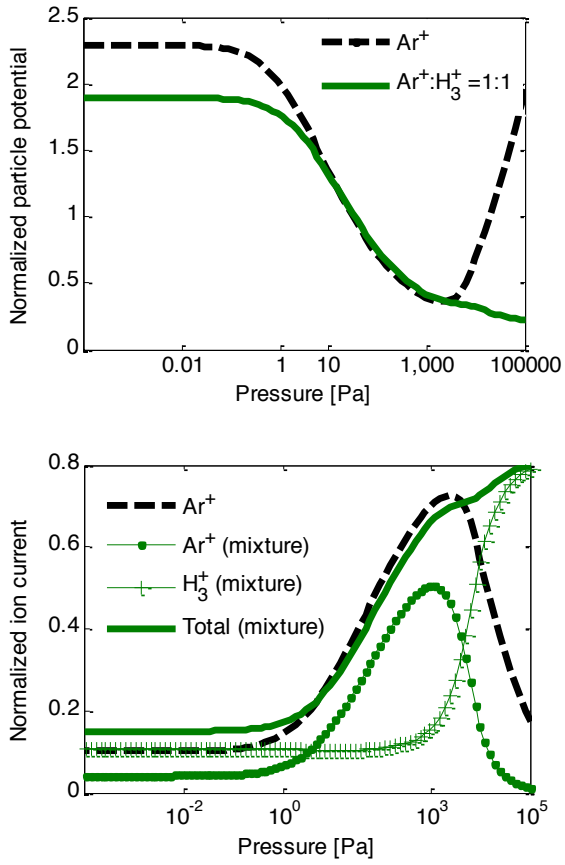

Figure 6: Potential of a 200 nm particle and ion currents as functions of pressure.

The result of parameterizing the ion ratio, gradually replacing Ar^+ ions with H_3^+ ions causes the particle potential to behave as shown in Figure 7. With increasing H_3^+ ion fraction in pure Ar gas, the potential gets lower in the low pressure regime. However, in the intermediate pressure range, it becomes slightly higher. This is because the currents, dominated by collision enhanced Ar^+ ions, become weaker as the fraction of H_3^+ ions is increased. At higher pressures, the collision enhanced H_3^+ ion current peaks and dominates the total current.

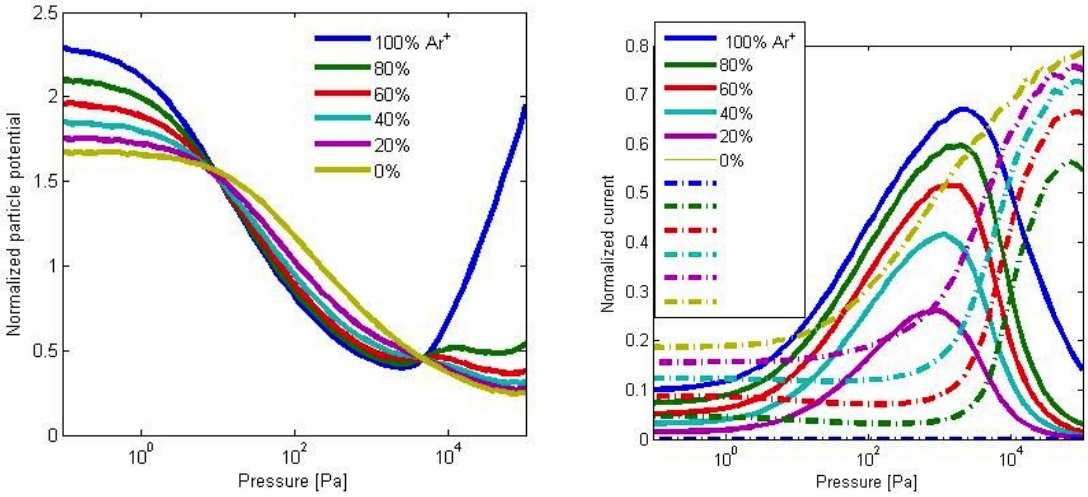

Figure 7: Potential versus pressure with ion fractions as a parameter.

A direct Monte-Carlo (MC) simulation was performed to validate the results from the analytical model. The interaction of H_3^+ with argon gas is only via elastic scattering. We used a model for collision cross sections, which suggests that elastic scattering has the largest cross section at low energies, among the cross sections of interaction between H_3^+ ion and argon gas. The presence of hydrogen gas was neglected based on the assumption that its ratio is small compared to argon neutral gas. Figure 8 compares the MC with the analytical model for two different ratios of H_3^+ and Ar^+.

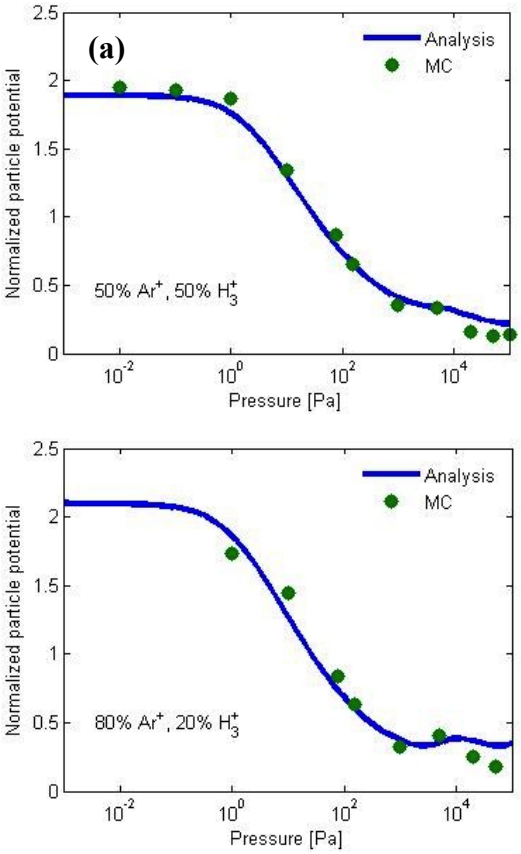

Figure 8: Comparison of analytical and Monte Carlo simulation for different ion fraction of Ar^+ and H_3^+ (a) 1:1 and (b) 4:1.

The MC simulations also support our contention that Ar^+ and H_3^+ ion currents peak at different pressures, causing the particle potential to remain low over a wide range of pressures. Figure 9 shows the ion fluxes against potential.

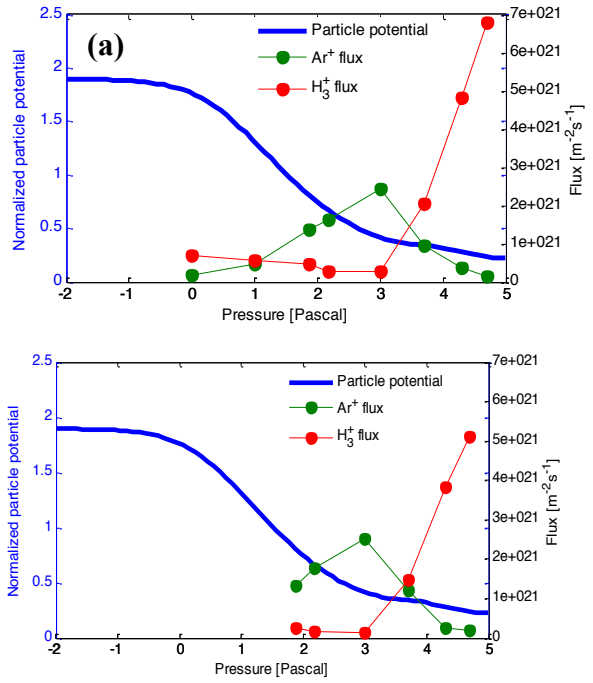

Figure 9: Ion fluxes and particle potential for Ar^+:H_3^+ ratios, (a) 1:1 and (b) 4:1.

The particle potential affects the energy with which ions impinge on its surface. The distribution of ion energy transferred to the particle surface is a function of both gas pressure and surface potential. The effect of the presence of triatomic hydrogen is best understood by comparing the ion energy distribution (IED) of Ar^+ ions when they are solely present in argon gas, with that of 1:1 ratio of Ar^+ and H_3^+ ions in argon gas. Figure 10 compares the two cases at low, medium and high pressures. At low pressures, there is only a little difference in the ion energy distribution. At medium pressures, the high energy tail of Ar^+ is replace by lower energy distributions of Ar^+ and H_3^+. The biggest difference is seen in the high pressure regime. This would have implications on the particle surface chemistry.

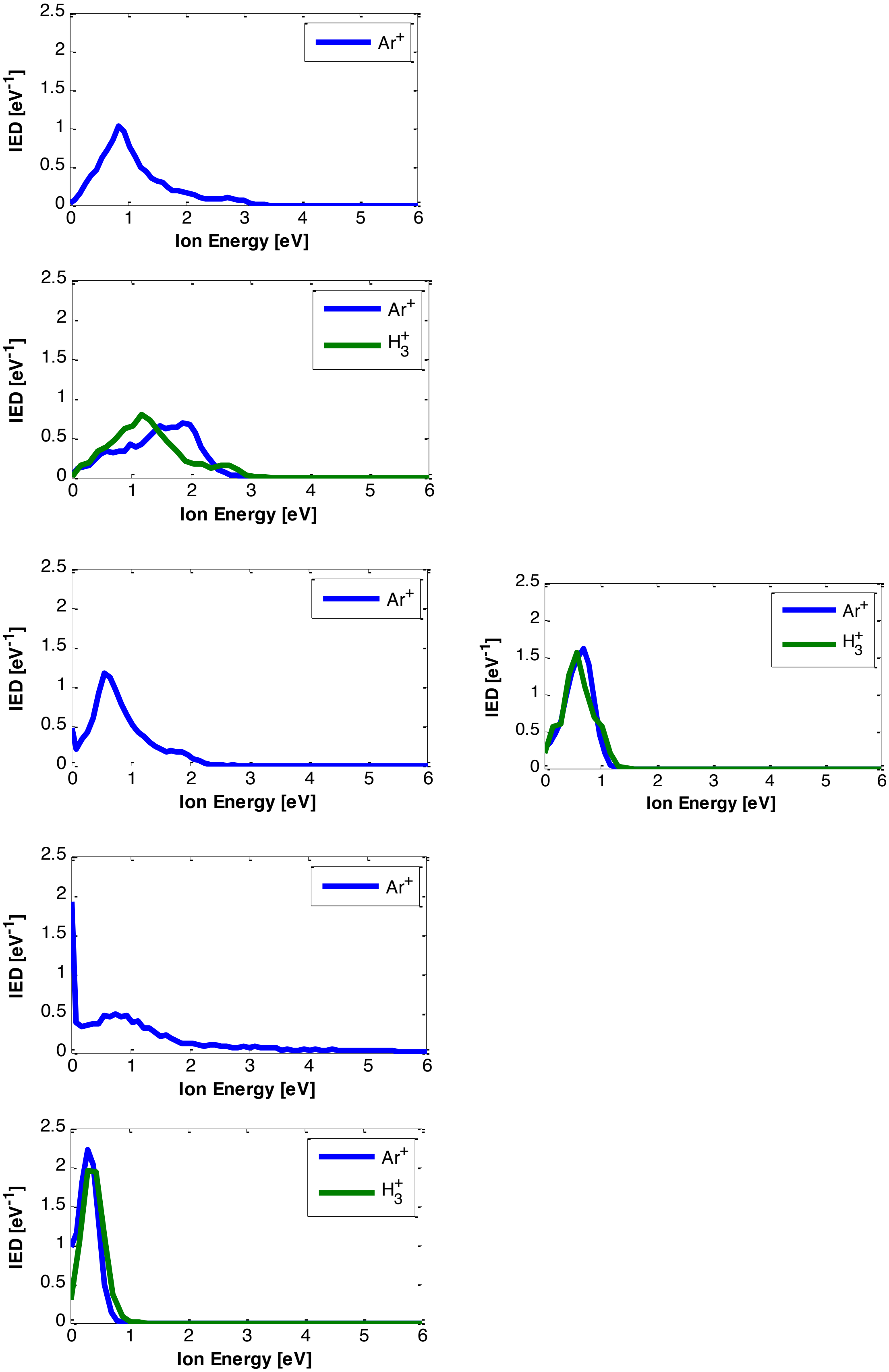
IED [eV^-1]
Ion Energy [eV]
Ar+
H3+

Figure 10: Ion energy distributions for 0.5 Torr (row 1), 37.5 Torr (row 2), 150 Torr (row 3) for a 200 nm particle in single ion environment of Ar^+ (1 x 10^{16} m^{-3}) on the left column and a mixture of Ar^+ (5 x 10^{15} m^{-3}) and H_3^+ (5 x 10^{15} m^{-3}) on the right column.

References

1. Marco Gatti; Kortshagen, U. *Analytical Model of particle charging in plasmas over a wide range of collisionality.* Physical Review E, **2008,** *78* (4), 046402.

2. Allen, J. E. *Probe theory - The orbital motion approach.* Physica Scripta, **1992,** *45*, 497.

Appendices

The energy distribution function of ions impinging on nanoparticles in a collisional low-pressure plasma

2012 Plasma Sources Sci. Technol. 21 035002

(http://iopscience.iop.org/0963-0252/21/3/035002)

Plasma Sources Sci. Technol. **21** (2012) 035002 (8pp) doi:10.1088/0963-0252/21/3/035002

The energy distribution function of ions impinging on nanoparticles in a collisional low-pressure plasma

Federico Galli, Meenakshi Mamunuru and Uwe R Kortshagen

Department of Mechanical Engineering, University of Minnesota, 111 Church St. SE, Minneapolis, 55455 MN, USA

E-mail: federico@me.umn.edu, mamun001@umn.edu and kortshagen@umn.edu

Received 28 November 2011, in final form 26 March 2012
Published 3 May 2012
Online at stacks.iop.org/PSST/21/035002

Abstract
A self-consistent particle-in-cell/Monte Carlo collision (PIC/MCC) simulation is used to calculate the ion energy distribution (IED) function of ions impinging on the surface of nanoparticles in low-pressure argon plasmas. The computation includes the effects of resonant charge-exchange and elastic collisions between ions and neutrals through a Monte Carlo null-collision method and considers both Maxwellian and non-Maxwellian electron energy distributions. Results show a strong dependence of the IED on pressure. Intermediate pressures yield a remarkable reduction in the average ion energy and an enhancement in the ion flux to the surface of the nanoparticles.

(Some figures may appear in colour only in the online journal)

1. Introduction

Over the last two decades radio-frequency low-pressure plasmas have been increasingly used as a medium to produce crystalline nanometer-sized semiconductor particles. The unique properties of these plasmas allow for the production of good quality nanocrystals with high yield, high degree of crystallinity and a very narrow size distribution [1–4]. Dusty low-pressure plasmas are complex, non-linear, non-equilibrium systems and the excellent results obtained in nanocrystal synthesis strongly rely on the complex interactions between plasma species (electrons, ions and neutrals) and the nanoparticles. Energetic electrons are capable of initiating very fast chemical kinetics [5–9]. At the same time, the mobile electrons are collected on surfaces with a greater efficiency than the colder ions. This results in nanoparticles carrying on average a negative charge [10, 11]. The unipolar charging of particles in the plasma prevents agglomeration and is crucial for achieving a monodisperse nanocrystal size distribution. Furthermore, the charging contributes to the creation of a local electric field that accelerates ions, increasing their flux toward the surface of the particles. Ions can carry a considerable amount of kinetic energy and, in contrast to neutrals, can enhance or induce processes such as surface species migration, displacement of surface and bulk atoms, and sputtering [12, 13]. The enhancement of the ion flux caused by the electric field and the energy exchange resulting from the ion neutralization at the surface of the particle contribute to heating and favor crystallization [14].

The charging models of nanoparticles in low-pressure plasmas were developed along the lines of probe theories and for a long time collisionless orbital motion limited (OML) theory was considered the state of the art [11, 15–17]. More recently, work has been done to show that the collisionless assumption made in the OML theory is seldom verified for ions [18–20]. Even when the mean free path of ions is considerably larger than the linearized Debye length, collisions between ions and neutrals from the background gas strongly affect ion collection [21–23] and the ion energy distribution (IED). While the effect of collisions on charging has now been widely studied and even the contribution of trapped ions to the IED in the sheath surrounding the particle was discussed [33], to our knowledge, the effects of collisions on the IED of ions hitting the surface of nanoparticles have not been systematically investigated. Since the synergistic interactions between plasma and surface species enable unique surface reactions and processes and because of the strong interest in understanding the effects of plasma species on the properties

of the nanoparticles, this paper studies the effects of charge-exchange and elastic collisions on the shape of the energy distribution of ions impinging on the surface of nanoparticles in low-to-intermediate pressure plasmas.

Another issue that has to date not been considered is the effect of non-Maxwellian electron energy distribution functions (EEDFs). It is not satisfactory to assume a Maxwellian EEDF and *a priori* speculate that the deviation from Maxwellian behavior will not affect the results. Hence, in this work both the cases of a Maxwellian and a non-Maxwellian EEDF are considered.

While little or no theoretical work was done in understanding the effects of pressure on the IED of ions hitting nanoparticles, the dusty plasma community is becoming sensitive to this issue. For example it is well understood that the suppression of high-energy ion bombardment is essential for the growth of crystalline diamond nanoparticles [24]. Morfill and co-workers reported on the 3D radio-frequency chemical vapor deposition of diamond grains where the 'substrate' consisted of seed particles levitated in a plasma composed of a mixture of CH_4 and H_2 [25] . They suggest that in high-quality CVD diamond growth the impinging ion energy should be minimized.

While there are no studies of the effect of pressure and collisions on the IED in nano-dusty plasmas, some lessons may be learned from studies of the influence of ion energies on the growth of amorphous and crystalline silicon thin films. Van de Sanden's group investigated the effects of different IEDs on the growth and properties of a-Si : H (amorphous hydrogenated silicon) thin films using external rf substrate bias (ERFSB) techniques in a remote $Ar/H_2/SiH_4$ expanding thermal plasma [26, 27]. The authors showed that low-energy ions activate ion-surface processes that cause Si surface atom displacements, intermediate-energy ions also cause Si bulk atom displacement, while high-energy ions provide significant Si atom sputtering. With respect to nanoparticle–plasma interactions, this study suggests that low-energy ions may be important in reducing the defect density, and improving the overall quality of the nanocrystals produced. In other work, Humbird and Graves [28, 29] performed a computational study on the interactions of energetic argon ions with silicon surface atoms using molecular dynamics simulations. They showed how the energy and the flux of argon ions to the surface determines the phase of a silicon substrate: high-energy ions are able to destroy the crystalline order and create an amorphous layer, while low-energy ions can 'heal' the damage and promote the formation of crystalline material.

As there is now significant interest in understanding the mechanisms that lead to nanocrystal formation in plasmas, it appears imperative to understand the formation of the IED of ions hitting nanoparticles suspended in a plasma. This is the topic of this paper. The studies presented here are a first step toward understanding the detailed plasma–nanoparticle interactions that lead to the formation of nanocrystals.

2. Description of the simulation

In this study, we used a self-consistent particle-in-cell/Monte Carlo collision (PIC/MCC) simulation for the ions in the sheath around the nanoparticles. The simulation is similar to the one developed by Gatti and Kortshagen [23]. The problem is simplified by assuming spherical symmetry around the particle, making the simulation one-dimensional. The equation of motion is solved for the ions in the simulation domain. Collisions of ions with neutrals are treated with a Monte Carlo approach. Electrons are described with a continuum approach. The electric field and the potential profile around the particle is determined by integration of the Poisson equation over the instantaneous charge distribution.

The simulation domain extends to five linearized Debye lengths λ_D from the particle surface. For our plasma conditions $\lambda_D = [e^2 n_0/(\varepsilon_0 k_B) \times (T_e^{-1} + T_i^{-1})]^{-1/2} \approx 12\,\mu$m, with e the elementary charge, k_B the Boltzmann constant, ε_0 the vacuum permittivity, n_0 the unperturbed plasma density, and T_e and T_i the electron and ion temperatures, respectively. The simulation domain is divided into 1000 radial cells with a slightly exponentially increasing cell size with growing distance from the particle surface. The minimum cell size is 10 nm.

For a given potential profile, the ion trajectory between collisions is determined with a velocity Verlet algorithm [34]. A continuously updated record is kept of ion positions, velocities, angular momenta and collision times. The collision times are calculated from the maximum collision frequency as a function of energy. When the simulation time matches the collision time for a given ion, a null-collision Monte Carlo method [32] is applied to determine the nature of the collision (real or null) and a new collision time is calculated. This approach allows for a collision dynamics that is consistent with the energy dependence of the collision cross sections. In the event of a real collision, the ion velocity and angular momentum are updated. In a charge-exchange collision event a stochastic neutral velocity and angular momentum are assigned to the ion, with neutral gas atoms assumed have a Maxwellian distribution. In the event of an elastic collision, random collision angles are generated and the new ion properties are calculated. The collisions can affect both the electric field around the particle and more significantly the energy of ions reaching the surface of the nanoparticle. As the ion motion is continuously tracked, 'trapped' ions that are on a closed orbit around the particle are self-consistently accounted for in the simulation. Their effect on electrostatic shielding of the particle and the charged species fluxes to the surface of the particle is intrinsically part of the simulation [33]. Ions leaving the simulation domain or being absorbed by the nanoparticle are replaced by ions entering the simulation domain, which are assumed to have a Maxwellian energy distribution in the unperturbed plasmas.

Electrons have a much smaller mass and a much larger velocity; differently from what is done in a particle-in-cell simulation [35] it would be impractical here to treat the individual motions of electrons similar to those of ions. Hence, a continuum approach is adopted for the electrons. The electron fluxes to the nanoparticle are derived assuming Boltzmann distributed electrons in the case of a Maxwellian

and an equivalent distribution for non-Maxwellian electrons:

$$\Gamma_{\mathrm{e,Max}} = \pi a^2 n_0 v_{\mathrm{th,e}} \exp\left(\frac{eV_\mathrm{p}}{k_\mathrm{B}T_\mathrm{e}}\right) \quad (1)$$

$$\Gamma_{\mathrm{e,non\text{-}Max}} = \pi a^2 n_0 \int_{-V_\mathrm{p}}^{\infty} \left(1 + \frac{V_\mathrm{p}}{\epsilon}\right) \sqrt{\frac{2e\epsilon}{m_\mathrm{e}}} f_0(\epsilon)\sqrt{\epsilon}\,\mathrm{d}\epsilon. \quad (2)$$

Here Γ_e is the electron flux, a is the particle radius, v_th is the electron thermal velocity, V_p is the particle floating potential, m_e is the electron mass, f_0 is the electron energy probability function and ϵ the electron kinetic energy. The charge of the nanoparticle is updated always when the electron flux integrated over time reaches an integer value, accounting for the discrete nature of the electrical charge.

The potential $V(r)$ and electric field $E(r)$ in the simulation domain are found from the integration of the Poisson equation, even though deviations from a Coulomb potential close to the particle are very small since the nanoparticles considered here have radii $a \ll \lambda_\mathrm{D}$. The Poisson equation is solved subject to the boundary conditions that the electric field at the particle surface is $E(a) = -\mathrm{d}V/\mathrm{d}r|_a = eQ_p/(4\pi\varepsilon_0 a^2)$, with Q_p the number of elementary charges on the particle, and the potential at the outer boundary of the simulation domain is zero. Accordingly, the potential at the inner boundary coincides with the particle floating potential. The ion density is integrated from the instantaneous ion distribution while the electron density profile depends directly on the potential profile both in the Maxwellian and non-Maxwellian case:

$$n_{\mathrm{e,Max}}(r) = n_0 \exp\left(\frac{eV(r)}{k_\mathrm{B}T_\mathrm{e}}\right) \quad (3)$$

$$n_{\mathrm{e,non\text{-}Max}}(r) = n_0 \int_{-V(r)}^{\infty} f_o(\epsilon)\sqrt{\epsilon}\,\mathrm{d}\epsilon \quad (4)$$

As the electron density and the electric potential depend on each other, an iterative approach is adopted to find their self-consistent profiles. Since the effect of screening close to the particle is small for the nanoparticles considered here, this approach converges rapidly.

At the beginning of the simulation, an initial guess of the potential profile is made based on a shielded Yukawa potential assuming an initial particle charge. The domain is then filled with ions at the prescribed density and initially at room temperature. The initial ion population is allowed to relax in the initial Yukawa potential, which is held constant during the relaxation process. The simulation then switches to a full self-consistent mode. In this mode the ions are moved for a time step $\mathrm{d}t = 1$ ps and the Poisson equation is solved as described above. The time step of 1 ps is short enough to accurately resolve the ion motion even close to the nanoparticle. The simulation is allowed to proceed until a steady electric potential around the nanoparticle is found. Ions that leave the simulation cell through impacting on the particle surface contribute to the particle charge and their impaction velocities are registered. A histogram of collection frequencies against impact energy is created and updated for each charging event.

Input parameters to the simulation are the pressure, the diameter of the nanoparticle, the electron temperature for a Maxwellian EEDF or the EEDF in the case of a non-Maxwellian plasma, the ion/electron density (in all cases considered here equal to $1 \times 10^{10}\,\mathrm{cm}^{-3}$), the neutral/ion temperature (300 K or 0.025 eV), the ionic mass (argon), and the charge-exchange and elastic collision cross sections as a function of energy, obtained respectively from [30, 31]. Simulations were performed for a range of neutral pressures between 0.1 and 31 600 Pa, for particle sizes ranging from 10 nm to 1 μm in diameter. A parametric study of the effect of electron temperature and reduced electric field was also performed. For the Maxwellian case, electron temperatures between 2 and 6 eV were used while in the case of non-Maxwellian plasmas the electron energy distribution was generated from the solution of the Boltzmann equation provided by the BOLSIG solver [36]. In this Boltzmann solver the angular dependence of the velocity distribution function is expanded for the first two terms in Legendre polynomials while the energy dependence is expanded in finite elements (cubic B-splines) [37]. The EEDFs are assumed to be close to isotropic which is likely a good assumption for the relatively low E/N values considered here. The reduced electric field E/N used in these calculations ranged between 5 and 110 Td ($10^{-17}\,\mathrm{V} \times \mathrm{cm}^2$). Figure 1 contains plots of the EEDF for electrons either in a Maxwellian or a non-Maxwellian argon plasma. In the Maxwellian case the electron temperature is 3.4 eV while in the non-Maxwellian case the *effective* electron temperature is 3.4 eV and the reduced electric field is 10 Td. Note how the non-Maxwellian distribution decreases rather rapidly for energies above the inelastic collision thresholds, which may impact the particle floating potential.

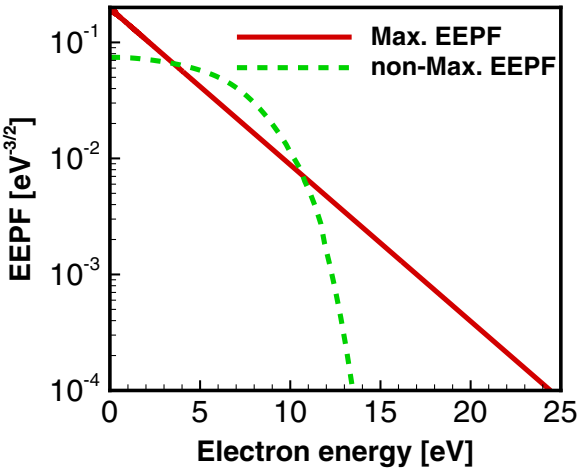

Figure 1. Plots of the electron energy probability function for the case of electrons in either a Maxwellian or a non-Maxwellian argon plasma with, respectively, an electron temperature of 3.4 eV and $E/N = 10$ Td.

3. Results

We start our discussion with examining the effects of different kinds of EEDFs and of the discharge pressure on the IED of ions impinging on nanoparticle surfaces. Figure 2 compares IEDs for both Maxwellian and non-Maxwellian distribution functions for a 500 nm particle in an argon plasma with

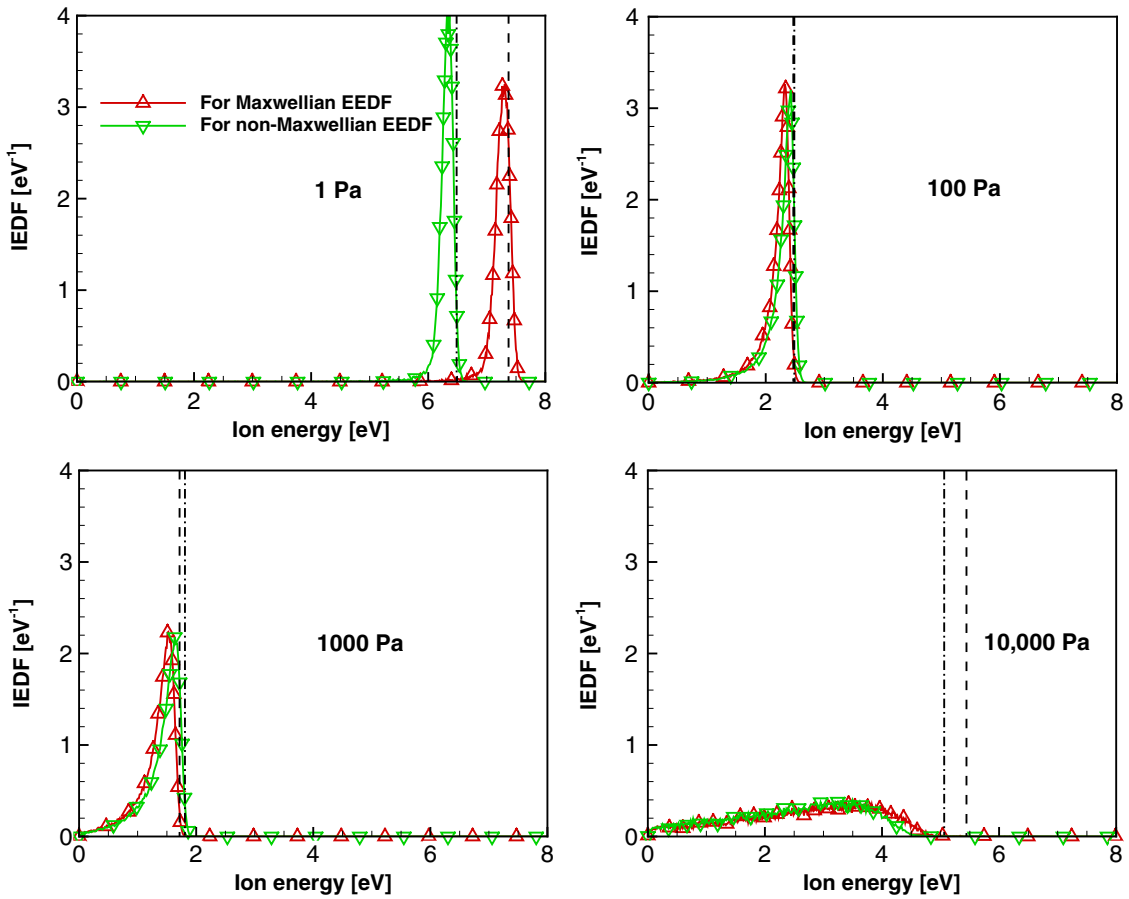

Figure 2. Results of simulations for the energy distribution of ions impacting a 500 nm particle, assuming either a Maxwellian or a non-Maxwellian electron energy distribution in argon plasma at $E/N = 10$ Td. $n_i = 1 \times 10^{16}$ m^{-3}, pressure range $P = 0.1$–$10\,000$ Pa. The effective electron temperature for both cases is 3.4 eV. The dashed line and the dotted–dashed line indicate particle potentials for Maxwellian and non-Maxwellian EEDFs, respectively.

$E/N = 10$ Td. The corresponding temperature of the Maxwellian EEDF, defined as 2/3 the mean kinetic energy of the non-Maxwellian EEDF, is 3.4 eV. Figure 2 reveals two important facts about the IEDs. First, for low pressures, the IEDs have a beam-like shape, suggesting that the ion motion in the sheath around the particle is collisionless. At the pressure of 1 Pa, a significant difference between Maxwellian and non-Maxwellian EEDFs is observed. The average energy of ions reaching the surface of the particle for a non-Maxwellian EEDF is approximately 1 eV lower than for the corresponding Maxwellian EEDF with the same effective electron temperature. At this low pressure the absolute value of the nanoparticle potential is 7–8 V and electrons in the tail of the distribution play a significant role in the charging of the nanoparticles. As a Maxwellian EEDF contains more electrons in the energetic tail than a non-Maxwellian EEDF, a more negative nanoparticle potential is required to balance the electron flux with the ion flux. This more negative potential causes a higher ion energy in the Maxwellian EEDF case. The second observation is that the IEDs show a significant dependence on the discharge pressure, even though the EEDFs remain unchanged, since the effective electric field E/N and electron temperature are held constant. This behavior is a reflection of the variation of the particle floating potential with discharge pressure. The particle floating potential changes strongly, since with increasing pressure the physical regime of ion collection changes, as discussed in detail in [23]. At low pressures, the ion motion in the Debye sphere around the particle is almost collisionless and ion collection is described by the collisionless OML theory [11, 15, 16]. At higher pressures, the ion collection by the particle is enhanced by collisions of ions within the Debye sphere. In this regime, known as the collision enhanced current regime, ions that would miss the particle if the motion were collisionless do get collected by the particle since their angular momentum was changed in a collision. This leads to an enhanced ion collection which causes a less negatively biased particle floating potential and thus reduced ion impact energies at the particle surface. As the particle becomes less negative, the relative importance of the EEDF tail decreases and the IEDs for the Maxwellian and non-Maxwellian EEDFs become almost identical. The IEDs also develop a low-energy tail, characteristic of ions that have undergone collisions within the sheath. As the pressure increases further, the ion motion in the particle sheath becomes strongly collisional, leading to a mobility dominated motion. In this 'hydrodynamic' regime, the nanoparticle potential again becomes more negative, since collisions reduce the ion current to the particle. However, since the ion motion is strongly collisional, the ion energies do not proportionally follow suit.

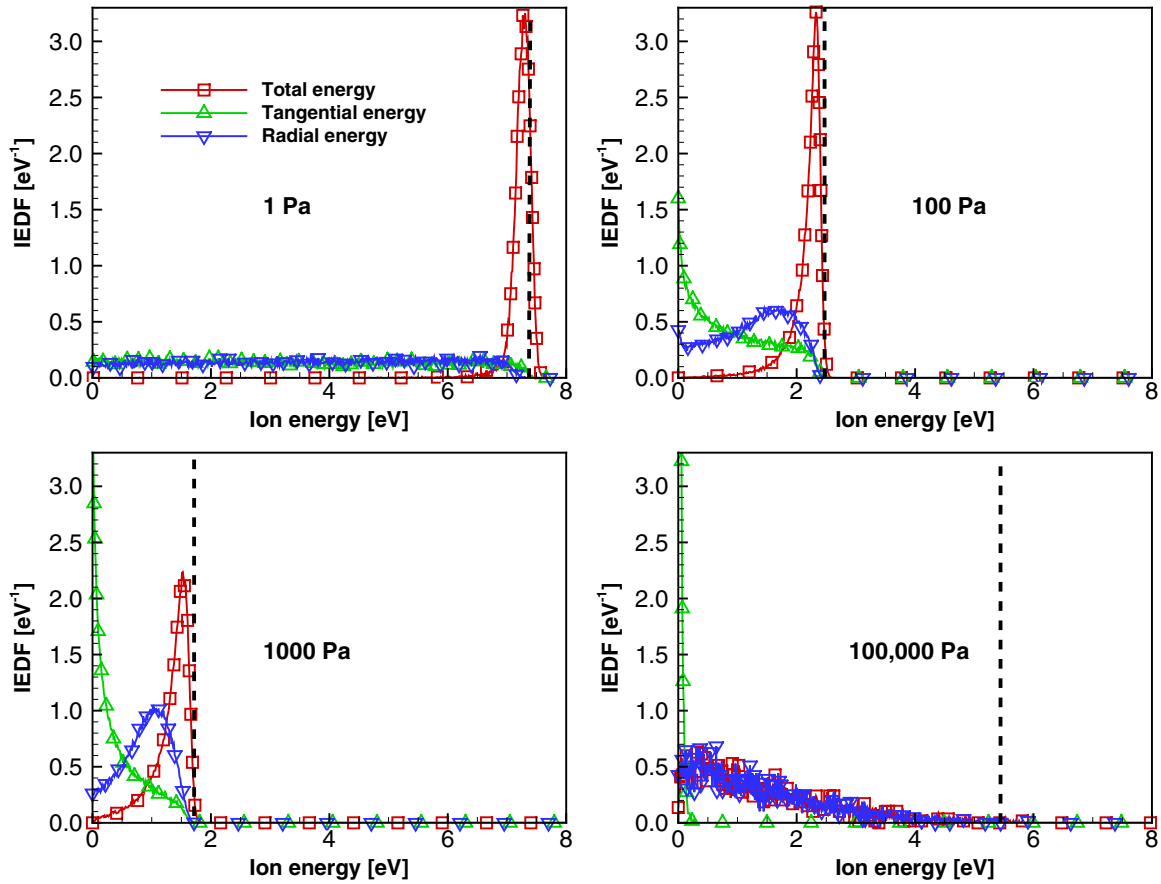

Figure 3. Results showing IED (and distributions of the energy associated with the radial and tangential ion velocity components) for 500 nm particles in diameter, assuming Maxwellian EEDF in argon plasma, for $P = 1$, 100, 1000 and 100 000 Pa, $T_e = 3.4$ eV, $n_i = 1 \times 10^{16}$ m^{-3} and $T_i = 300$ K. The dashed line indicates the absolute value of the particle potential.

In figure 3 we plot the distribution of kinetic energy carried by ions impinging on the surface of a nanoparticle; we further divide the energy based on the velocity direction distinguishing between the radial velocity component and the tangential velocity component of the impinging ions. We refer to the former as 'radial energy component' and the latter as 'tangential energy component'. In these plots the dotted line indicates the position of the particle floating potential on the energy axis. An ion reaching a nanoparticle with high tangential component and low radial component is essentially 'grazing' the surface of the particle, while an ion reaching with only radial component is having a collision with maximum momentum exchange. In the low pressure case, while all ions arrive with roughly the same total energy, there is a wide spread in the distributions of tangential and radial energies. As the pressure increases, the tangential energy component becomes less and less important and the ion motion becomes more and more radial as an effect of frequent collisions.

The effects of particle size on the IED for 500 nm particles and 50 nm particles are compared in figures 4 and 5, respectively. For the 500 nm particle, the particle potential becomes less negative and the ion energies decrease with increasing pressure up to about 320 Pa. At higher pressures the ion current enters the hydrodynamic regime causing a more negative particle potential and an increase in the ion energies. Only at the highest pressure of 31 600 Pa does the ion energy decrease again due to the highly collisional ion motion in the sheath. The 50 nm particle shows a qualitatively similar behavior; however, with a shift to higher pressures. For instance, the ion energies decrease up to a pressure of 10 000 Pa. This behavior is based on the fact that a smaller particle carries a smaller charge and is thus surrounded by a smaller Debye sphere. At the same pressure, the ion motion is more collisional in the larger sheath around the larger nanoparticle while still being less collisional in the smaller sheath around the smaller particle.

Figure 6 summarizes the findings of figures 4 and 5. It shows the mean and the mode for the IED as well as the predicted ion flux for the 500 nm and the 50 nm nanoparticle diameter, respectively. It is quite remarkable that in the 50 nm case the ion flux increases by almost a factor of 10 while the average ion energy drops from a value of about 7.5 eV to a value of 0.6 eV (a 12-fold reduction). It is also worth noting that in the OML regime and in the collision enhanced regime, the mean ion energy closely follows the particle potential; however, in the hydrodynamic regime it becomes much smaller than the particle potential.

In figure 7 we report the results of a parametric study on the effects of reduced electric field and the electron energy on the IED. While pressure is easily adjustable in experiments, the electron temperature adjusts in a self-consistent manner as determined by parameters such as

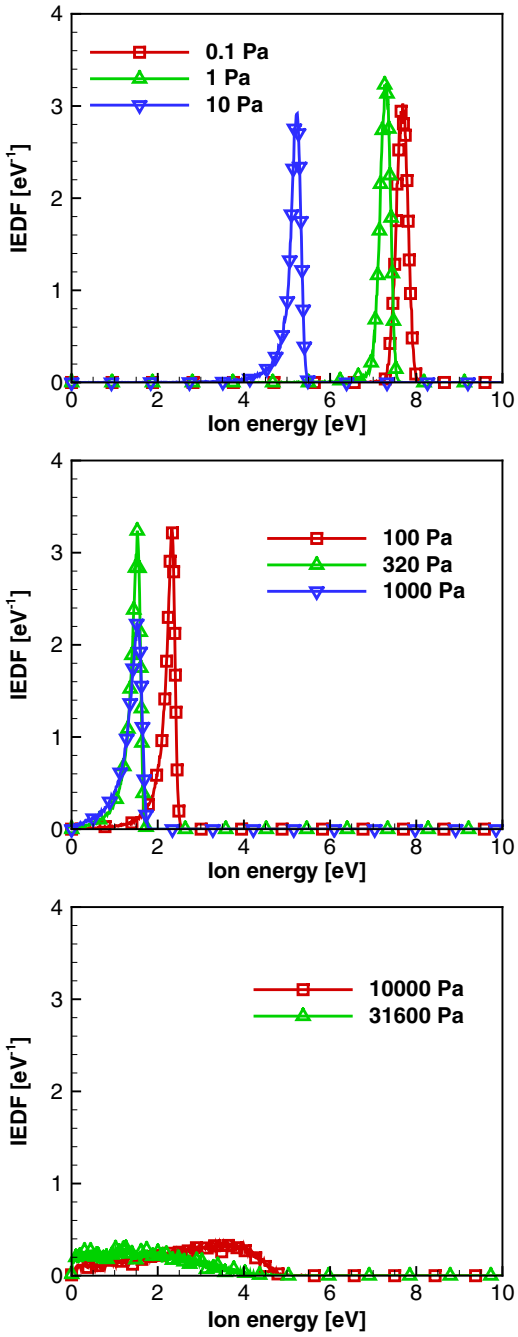

Figure 4. Results of simulations for the IED for 500 nm particles in a Maxwellian argon plasma, $n_i = 1 \times 10^{16}\,\mathrm{m}^{-3}$, $T_e = 3.4\,\mathrm{eV}$, pressure range $P = 0.1$–$31\,600\,\mathrm{Pa}$.

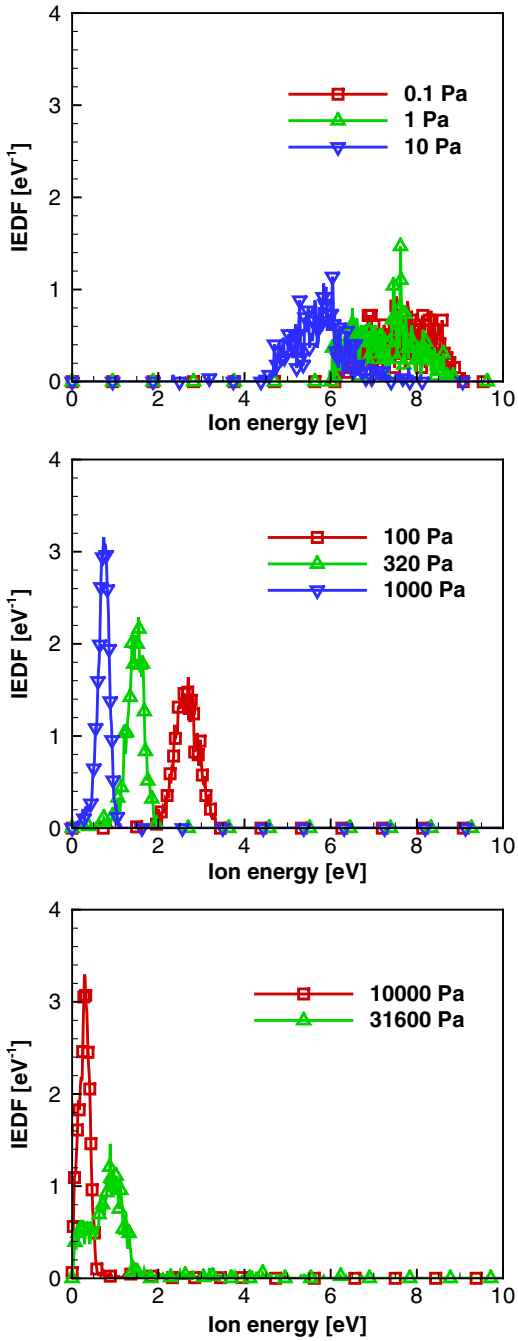

Figure 5. Results of simulations of the IED for 50 nm particles in a Maxwellian argon plasma, $T_e = 3.4\,\mathrm{eV}$, $n_i = 1 \times 10^{16}\,\mathrm{m}^{-3}$, pressure range $P = 0.1$–$31\,600\,\mathrm{Pa}$.

pressure, plasma composition, reactor geometry, and others. Furthermore, as we see from the results, the modifications of the IED due to changes in the electron temperature are not significant. Larger electron energies provide a slightly larger ion flux and average ion energy, but the changes are on the order of ≈10%.

At this point, it may be instructive to comment on the potential influence of the IEDs discussed here on the formation of nanoparticles in plasmas. It is worth noting that the literature reports of production of the best quality semiconductor nanocrystals from low-pressure plasmas use pressures that, according to our present results, coincide with an enhanced ion flux and a reduced ion energy [14]. As our results have shown, for small pressures ($P < 100\,\mathrm{Pa}$) there is a considerable fraction of ions with energies above the binding energy for Si–Si and Si–H surface species (≈3 eV) [38]; however, at larger pressures the particle potential becomes less negative and a large fraction of ions impinges at or below the binding energy. It may thus be expected that the IED of ions hitting the nanoparticles during growth plays an essential role, if ion flux is at least roughly on the order of the growth species flux of elementary silane radicals (e.g. SiH_x, $x = 1,2,3$).

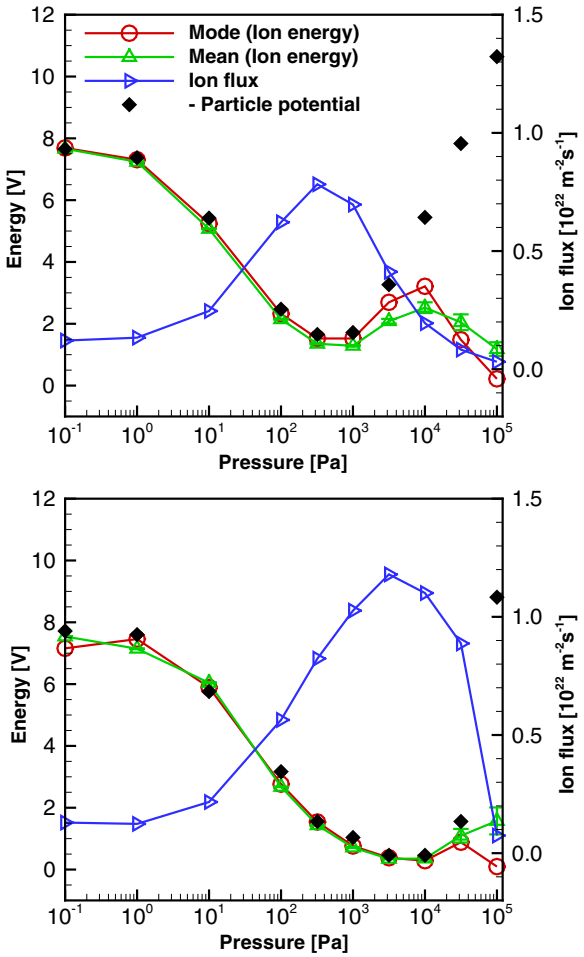

Figure 6. The absolute value of nanoparticle potential, the ion flux and the mean and mode for the energy of ions impinging on a 500 nm particle (above) and a 50 nm particle (below). Plasma parameters are as reported in figures 4 and 5. Notice the dramatic reduction in the average ion energy and the concurrent increase in the total flux taking place in the range of pressures commonly used for the synthesis of nano-crystalline materials in low-pressure dusty plasmas.

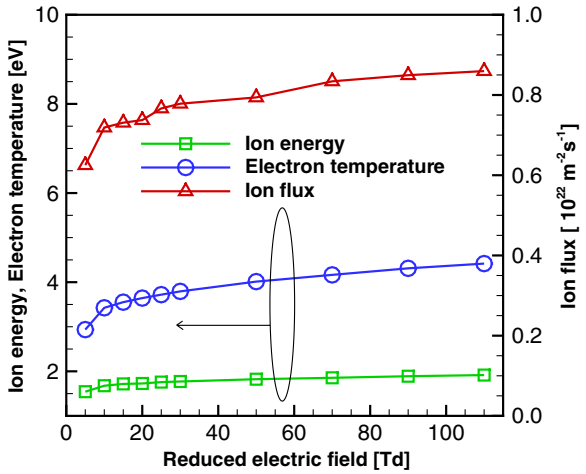

Figure 7. Effect of reduced electric field on the effective electron temperature, the average ion energy and the average ion flux for ions impinging on a 500 nm particle in a non-Maxwellian argon plasma at 200 Pa of pressure and an ion density of $n_i = 1 \times 10^{16}\,\mathrm{m}^{-3}$.

Mangolini *et al* [2] reported the growth of a 6 nm particle in a 7 ms residence-time in a flow-through reactor. Assuming a constant diameter growth rate this yields an average growth rate of about $0.85 \times 10^{-6}\,\mathrm{m\,s}^{-1}$. One monolayer of silicon atoms $\rho_{\mathrm{Si}}^{\mathrm{monolayer}}$ contains 7×10^{18} atoms m^{-2} in the [100] direction. The monolayer spacing is then $(\rho_{\mathrm{Si}}^{\mathrm{monolayer}})^{-1/2} = 0.377$ nm. From the growth rate and the monolayer spacing we get to an estimate of the time required to add a layer of Si atoms to a Si particle, which is 4.4×10^{-4} s. The Si atom flux to achieve this growth rate is 7×10^{18} atoms $\mathrm{m}^{-2}/4.44 \times 10^{-4}$ s $\approx 1.6 \times 10^{22}$ atoms $\mathrm{m}^{-2}\mathrm{s}^{-1}$. The flux of ions for the same plasma parameters is on the order of 5×10^{21} ions $\mathrm{m}^{-2}\,\mathrm{s}^{-1}$. The ratio of the ion to monomer flux is thus ≈0.3. This suggests that under the conditions considered by Mangolini *et al* [2] ions can play a significant role in the reorganization of silicon species newly attached to the nanoparticle surface, which may favor the formation of high-quality nanocrystals. A silicon monomer physisorbed or loosely bound to the surface of a particle may be affected by a collision with a low-energy argon ion. The interaction with the low-energy ion may allow the silicon atoms to find an energetically more favorable position on the particle surface leading to the formation of the crystalline phase. It is important that silicon atoms at the surface may experience such an interaction before a new monolayer of silicon atoms is deposited on the surface of the particle. Hence it is reasonable to assume that under conditions where the silicon growth species and the ion flux are on the same order, the optimal effect of the ions helping with the crystallization of the silicon nanoparticles is achieved.

4. Conclusions

In this paper, we have presented the results of a PIC/MCC simulation that evaluates the effects of resonant charge-exchange and elastic collisions between ions and neutrals on the ion energy distribution function of ions bombarding the surface of nanoparticles in collisional dusty plasmas in argon over a wide pressure range and both for the case of equilibrium and non-equilibrium electron populations. Results show that both the average ion energy and the total ion flux are a strong function of pressure. At low pressures, the shape of the EEDF has some influence on the IED, but this becomes less pronounced for higher pressures. A minimum in the ion energy and a maximum in the ion flux appear in the same narrow range of pressures that lead to collisional enhancement of the ion current (≈100–1000 Pa for a 500 nm particle) that are routinely adopted in the production of high-quality nano-crystalline semiconductors for photovoltaics and micro-electronics applications. Under these conditions, the nanoparticles are hit by a flux of ions, whose energy is too small to break Si–Si bonds at the particle surface. However, these ions may aid the reorganization of silicon atoms at the nanoparticle surface. We find that for conditions typically used for nanocrystal formation, the fluxes of silicon growth species and of ions are on the same order of magnitude, suggesting that ions play an important role in helping Si surface species to achieve the energetically most favorable surface location.

We thus suggest that the ion flux hitting the surface of the nanocrystals plays an important role in the crystallization of nanoparticles in plasmas.

Acknowledgments

This work was supported in part by the DOE Plasma Science Center for Predictive Control of Plasma Kinetics, which supported FG and URK. Partial support by the NSF/DOE Partnership in Basic Plasma Science through grants DOE/DE-SC0002391 and NSF CBET-0903842 is acknowledged, which provided support for MM and URK.

References

[1] Bapat A, Anderson C and Kortshagen U 2004 *Plasma Phys. Control. Fusion* **46** B97–109
[2] Mangolini L, Thimsen E and Kortshagen U 2005 *Nano Lett.* **5** 655–9
[3] Sankaran R M, Holunga D, Flagan R C and Giapis K P 2005 *Nano Lett.* **5** 537–41
[4] Giesen B, Wiggers H, Kowalik A and Roth P 2005 *J. Nanopart. Res.* **7** 29–41
[5] Shiratani M, Matsuo S and Watanabe Y 1991 *Japan. J. Appl. Phys.* **30** 1887
[6] Boufendi L and Bouchoule A 1994 *Plasma Sources Sci. Technol.* **3** 262
[7] Boufendi L, Hermann J, Bouchoule A, Dubreuil B, Stoffels E, Stoffels W W and Giorgi M L d 1994 *J. Appl. Phys.* **76** 148
[8] Bhandarkar U V, Swihart M T, Girshick S L and Kortshagen U R 2000 *J. Phys. D: Appl. Phys.* **33** 2731–46
[9] Bhandarkar U, Kortshagen U and Girshick S L 2003 *J. Phys. D: Appl. Phys.* **36** 1399–408
[10] Bernstein I B and Rabinovitz I N 1959 *Phys. Fluids* **2** 112
[11] Matsoukas T 1994 *J. Aerosol Sci.* **25** 599
[12] Kaufman H R and Harper J M E 2004 *J. Vac. Sci. Technol.* A **22** 221–4
[13] Takagi T 1984 *J. Vac. Sci. Technol.* A **2** 382–8
[14] Mangolini L and Kortshagen U 2009 *Phys. Rev.* E **79** 026405
[15] Allen J E, Annaratone B M and de Angelis U 2000 *J. Plasma Phys.* **63** 299–309
[16] Schweigert V A and Schweigert I V 1996 *J. Phys. D: Appl. Phys.* **29** 655
[17] Kortshagen U and Bhandarkar U 1999 *Phys. Rev.* E **60** 887
[18] Zobnin A V, Nefedov A P, Sinelshchikov V A and Fortov V E 2000 *J. Exp. Theor. Phys.* **91** 483–7
[19] Ratynskaia S *et al* 2004 *Phys. Rev. Lett.* **93** 085001
[20] Khrapak S A *et al* 2005 *Phys. Rev.* E **72** 016406
[21] Goree J 1992 *Phys. Rev. Lett.* **69** 277
[22] Lampe M, Gavrishchaka V, Ganguli G and Joyce G 2001 *Phys. Rev. Lett.* **86** 5278–81
[23] Gatti M and Kortshagen U 2008 *Phys. Rev.* E **78** 046402
[24] Shimizu S, Annarone B M, Shimizu T, Jacob W, Thomas H and Morfill G E 2008 *Plasma Sources Sci. Technol.* **17** 035014
[25] Shimizu T, Jacob W, Thomas H, Morfill G, Abe T, Watanabe Y and Sato N 2006 *Thin Solid Films* **506–507** 652–5
[26] Smets A H M, Kessels W M M and van de Sanden M C M 2007 *J. Appl. Phys.* **102** 073523
[27] Gevers P M, Gielis J J H, Beijerinck H C W, van de Sanden M C M and Kessels W M M 2010 *J. Vac. Sci. Technol.* A **28** 293–301
[28] Humbird D H and Graves D B 2002 *Plasma Sources Sci. Technol.* **11** A191–5
[29] Humbird D H and Graves D B 2002 *Pure Appl. Chem.* **74** 419–22
[30] Popescu-Iovitzu I and Ionescu-Pallas N J 1959 *Proc. Phys. Soc.* **75** 807
[31] Phelps A V 1991 *J. Phys. Chem. Ref. Data* **20** 557
[32] Kortshagen U, Parker J G and Lawler J E 1996 *Phys. Rev.* E **54** 6746–61
[33] Lampe M, Goswami R, Sternovsky Z, Robertson S, Gavrishchaka V, Ganguli G and Joyce G 2003 *Phys. Plasmas* **10** 1500–13
[34] Bagchi K, Andersen H C and Swope W 1996 *Phys. Rev. Lett.* **76** 255–8
[35] Choi S and Kushner M 1994 *IEEE Plasma Sci.* **22** 138–50
[36] Http://www.siglo-kinema.com/bolsig.htm
[37] Pitchford L C, ONeil S V and J R Rumble J 1981 *Phys. Rev.* A **23** 294–304
[38] Herak T, Chau T, Mejia S, Shufflebotham P, Schellenberg J, Card H, Kao K and McLeod R 1987 *J. Non-Crystal. Solids* **97–98** 277–80

Plasma-induced crystallization of silicon nanoparticles

IOP Publishing Journal of Physics D: Applied Physics

J. Phys. D: Appl. Phys. **47** (2014) 075202 (8pp) doi:10.1088/0022-3727/47/7/075202

Plasma-induced crystallization of silicon nanoparticles

N J Kramer[1], R J Anthony[1,2,3], M Mamunuru[1], E S Aydil[2] and U R Kortshagen[1]

[1] Department of Mechanical Engineering, University of Minnesota, 111 Church St. SE, Minneapolis, MN 55455, USA
[2] Department of Chemical Engineering and Materials Science, University of Minnesota, 421 Washington Ave. SE, Minneapolis, MN 55455, USA
[3] Department of Mechanical Engineering, Michigan State University, 428 S. Shaw Lane, East Lansing, MI 48824, USA

E-mail: nkramer@umn.edu and kortshagen@umn.edu

Received 8 October 2013, revised 11 November 2013
Accepted for publication 17 December 2013
Published 23 January 2014

Abstract

While the formation of nanoparticles in nonthermal plasmas is well known, the heating mechanism leading to their crystallization is poorly understood. In this study, we investigate the crystallization of amorphous silicon nanoparticles in nonthermal plasmas using a tandem plasma configuration. Amorphous silicon nanoparticles with diameters of 3, 4 or 5 nm are formed in a low-power nonthermal upstream plasma, and injected directly into a second separate downstream plasma. Crystallization of the amorphous silicon nanoparticles is investigated as a function of the power used to maintain the second plasma. This approach allows for the decoupling of nanoparticle synthesis and heating. The nanoparticle properties and plasma conditions are examined to obtain a comprehensive understanding of nanoparticle heating and crystallization. The particle crystallinity was studied using x-ray diffraction, Raman spectroscopy, and transmission electron microscopy. We discovered a threshold power for complete crystallization of the particles. A combination of comprehensive plasma characterization with a nanoparticle heating model reveals the underlying plasma physics leading to crystallization. Here we found that the nanoparticles reach temperatures as high as 750–850 K in the secondary plasma, which is well above the gas temperature and sufficient for complete nanoparticle crystallization. While we demonstrate this method of predicting nanoparticle temperature using silicon, the approach can be applied broadly to other plasma-synthesized nanomaterials.

Keywords: plasma physics, nanoscale science and low-D systems

S Online supplementary data available from stacks.iop.org/JPhysD/47/075202/mmedia

(Some figures may appear in colour only in the online journal)

1. Introduction

Using low-pressure nonthermal plasmas for the synthesis of silicon, germanium and indium phosphide nanoparticles is well-established [1–7]. Electrons in nonthermal plasmas can reach temperatures as high as 5 eV, and can dissociate molecular precursors such as silane and silicon tetrachloride upon collision to form reactive radicals [6, 8]. These radicals react to nucleate and grow nanometre sized particles. The nanoparticles formed in nonthermal plasmas tend to be negatively charged due to the significantly larger mobility and temperature of the electrons compared to the heavier positive ions [9–11]. The negative charge on the particles reduces agglomeration and coalescence significantly [12, 13], leading to much narrower and well-defined particle size distributions compared to other aerosol-based nanoparticle synthesis processes. Moreover, charging reduces, and even eliminates, diffusion losses to the walls of the reactor [14].

The residence time of the particles in the plasma offers excellent control of the particle size [1]. Depending on the synthesis conditions, the nanoparticles can be amorphous or crystalline [15].

The ability to produce crystalline group IV and III–V materials makes plasma synthesis an attractive method. However, one aspect of the plasma synthesis technique that is still poorly understood is nanoparticle heating, which is believed to be necessary for the formation of crystalline particles. Obtaining crystalline particles is critical for many optical and electronic applications, since amorphous particles typically have higher defect densities and charge carrier trap states, which are often detrimental to the electronic and optical properties of nanomaterials [15]. Moreover, knowledge of the nanoparticle temperature is critical for the successful incorporation of dopants into nanoparticles [16, 17].

While the melting and crystallization temperatures are lower for nanoparticles compared to their bulk counterparts [18], nanoparticles of covalently bonded semiconductors still require relatively high temperatures for crystallization. For instance, a recent study showed that crystallization of 4 nm, 6 nm, 8 nm and 10 nm diameter silicon nanoparticles requires temperatures of 773 K, 1073 K, 1173 K and 1273 K, respectively [19]. In a different study, crystallization temperatures for silicon particles larger than 10 nm were reported to be higher than 1047 K [20]. In contrast, the gas temperature in nonthermal plasmas is only 300–500 K [1], well below the temperatures required for crystallization, even for the smallest nanoparticles. Thus, the nanoparticles must be heated by the plasma to several hundreds of Kelvin above the gas temperature in order to crystallize. While several groups reported that it is possible for particles to exceed the gas temperature in plasmas [21–23], these temperatures were still not sufficient for crystallization of silicon nanoparticles.

Previously, we demonstrated an increase in silicon nanoparticle crystallinity with increasing power delivered to the plasma [15], which suggests that increasing nanoparticle temperature is responsible for crystallization. However, possible nanoparticle heating mechanisms have thus far only been investigated through computational models [11, 24, 25]. These studies found that the temperature of small (<5 nm) nanoparticles never reaches a steady state on the scale of the residence time, and that their temperatures can frequently spike to more than 1000 K. However, when the nanoparticles grow larger (>5 nm), the magnitude of the temperature spikes reduces significantly and the particle temperature can reach steady state.

In situ measurement of the nanoparticle temperature in a plasma is difficult, but the nanoparticles themselves can serve as thermometers, as their crystallinity and surface will change depending on the conditions they experience in the plasma. Here we present an approach that combines detailed plasma characterization with modelling to elucidate the heating mechanisms that lead to nanoparticle crystallization. In this approach, amorphous silicon nanoparticles are produced in a low-power plasma and subsequently injected into a second variable-power plasma. Hereafter, the first plasma used to synthesize the amorphous nanoparticles is also referred to as the primary plasma while the second plasma used to crystallize the nanoparticles is referred to as the secondary plasma. This approach decouples the nanoparticle synthesis and nanoparticle heating. The nanoparticle size can be varied by changing the synthesis conditions in the first plasma; this allows the investigation of the crystallization process for different nanoparticle sizes.

2. Experimental details

2.1. Nanoparticle synthesis

Silicon nanoparticles are formed in a continuous-flow low-pressure plasma reactor from an argon–silane–helium gas mixture, as described in detail previously [1]. The reactor consists of a borosilicate glass tube through which the reactant gases flow (argon and 5% silane diluted in helium). Figure 1(*a*) shows a schematic of the experimental setup. We supplied radio frequency (rf) power at 15 W and 13.56 MHz to ring electrodes in the upper region of the glass tube to form the amorphous silicon nanoparticles. The size of the particles is controlled by adjusting the flow rate of argon gas through the reactor tube between 18 and 60 standard cubic centimetres per minute (sccm) while maintaining a constant pressure of 200 Pa. For example, the nanoparticle size is decreased by increasing the argon flow rate and consequently the argon-to-silane ratio in the plasma while the pressure and silane flow rate are kept constant. This decreases the residence time of the nanoparticles in the plasma and the partial pressure of silane, leading to the formation of smaller nanoparticles. The silane (5% diluted in helium) flow rate is kept constant at 5 sccm while the argon flow rate is set to 18 sccm, 35 sccm and 60 sccm to form 5 nm, 4 nm and 3 nm nanoparticles, respectively. The size distributions are relatively monodisperse, with a typical standard deviation of 10% [1]. An overview of the plasma conditions can be found in table 1.

A second electrode in the lower half of the glass tube creates a second plasma with powers ranging from 5 to 50 W, as read from the power supply. The actual plasma power will be lower due to losses in the matching network. The second plasma will couple directly to the grounded flange of the reactor. An orifice downstream of the second plasma controls the pressure and accelerates the nanoparticles into the nanoparticle collection region. A glass substrate placed at the end of a moveable pushrod and positioned below the orifice collects the nanoparticles. This substrate can be pulled into an enclosure without breaking vacuum, which allows for air-free transportation of the nanoparticles. Agglomeration of the nanoparticles is avoided by reducing the distance between the two plasmas without overlapping them. If the distance between the two plasmas is too large, the nanoparticles lose their charge and agglomerate. When the secondary plasma power is sufficiently high, these agglomerates can coalesce due to the high nanoparticle temperature leading to an apparent growth of the particles in the second plasma [26]. When all of the silane gas is consumed in the primary plasma and agglomeration is minimized, the particle size does not change in the secondary plasma.

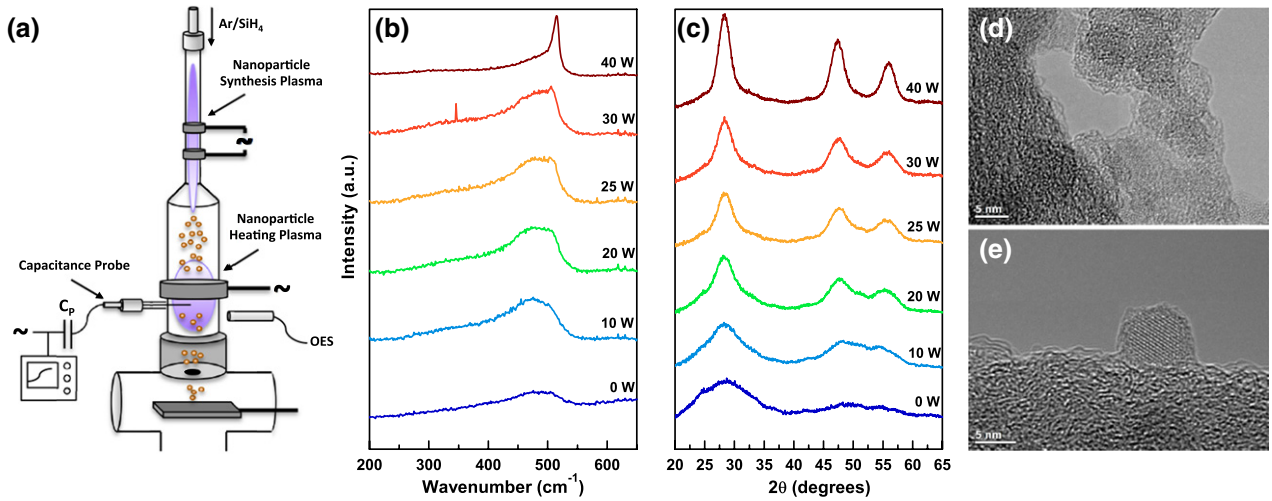

Figure 1. (*a*) Schematic of the tandem plasma experiment used to study silicon nanoparticle crystallization. Amorphous silicon nanoparticles are formed in a low-power synthesis plasma, followed by heating in a variable-power secondary plasma. Optical emission spectroscopy and capacitance probe measurements are used to determine the properties of the secondary plasma used for heating the nanoparticles. (*b*) Raman spectra from 4 nm nanoparticles as a function of power applied to the secondary plasma. At a critical power of 30 W the crystalline silicon feature at 520 cm^{-1} emerges. (*c*) X-ray diffraction from 4 nm nanoparticles exposed to the secondary plasma as a function of secondary plasma power. Diffractions for silicon nanocrystals emerge when the plasma power exceeds 30 W. (*d*) Transmission electron micrographs of 5 nm diameter silicon nanoparticles when the secondary power is off. This yields amorphous nanoparticles. (*e*) Crystalline nanoparticles are observed in TEM once the secondary plasma power is increased to 40 W.

Table 1. Overview of the plasma conditions for synthesizing 3, 4 and 5 nm nanoparticles in the primary plasma.

Nanoparticle size (nm)	Argon (sccm)	He/SiH_4 (5%) (sccm)	Pressure (Pa)	Primary plasma power (W)	Secondary plasma residence time (ms)
3	60	5	180	15	2.8
4	35	5	190	15	4.6
5	18	5	195	15	8.3

2.2. Nanoparticle characterization

X-ray diffraction (XRD) from nanoparticles was collected using a Bruker-AXS Microdiffractometer with a 2.2 kW sealed Cu x-ray source. The nanoparticle diameter is calculated from the Scherrer equation. Raman scattering from the nanoparticles was collected with a Witec alpha300 R confocal Raman microscope, UHTS300 spectrometer and DV401 CCD detector. An Omnichrome argon ion laser with 514.5 nm excitation and 50 mW maximum output power illuminated the sample. Nanoparticles collected on lacy-carbon grids were examined with a Tecnai G2 F30 transmission electron microscope (TEM).

2.3. Plasma analysis

The heating and cooling reactions on the nanoparticle surface are displayed schematically in figure 2. These reactions depend on the electron temperature, hydrogen density and ion density. Ion densities in the second plasma are measured using an electrostatic capacitive probe [27]. The probe consists of a 5.5 mm long, 0.8 mm diameter tungsten wire connected to a 1 nF capacitor. The probe is driven by an rf power supply at 1 MHz while the voltage of the capacitor is measured with an oscilloscope. The rf generator charges the capacitor through the negative self-biasing of the probe. The signal from the rf generator is periodically chopped, resulting in discharging of the capacitor from the positive ions collected by the probe. The rate at which the capacitor discharges is directly proportional to the ion flux [27, 28], and the ion density in the plasma can be calculated by assuming that the Bohm criterion relates the ion flux to the ion density. This approach is particularly useful for dusty plasmas, because deposition occurring on the probe itself does not affect the measurements [27, 28].

Optical emission from the second plasma is collected (see figure 1(*a*)) with an optical fibre connected to the entrance slit of a monochromator. A Corona model previously discussed in [24] and not repeated here was used to interpret the emission spectrum and to obtain the atomic hydrogen density. Briefly, this Corona model assumes that the excited states are populated via direct excitations from the ground states while depopulation occurs by radiative de-excitation. The hydrogen density in the plasma can be obtained by measuring the ratio of the hydrogen emission line intensity to the argon emission line intensities. The standard deviation of the hydrogen density is obtained by comparing the hydrogen densities calculated using multiple argon/hydrogen line ratios. The electron temperature is then estimated to be the value at which the overall standard deviation is minimum [29]. For more details the reader is referred to [24].

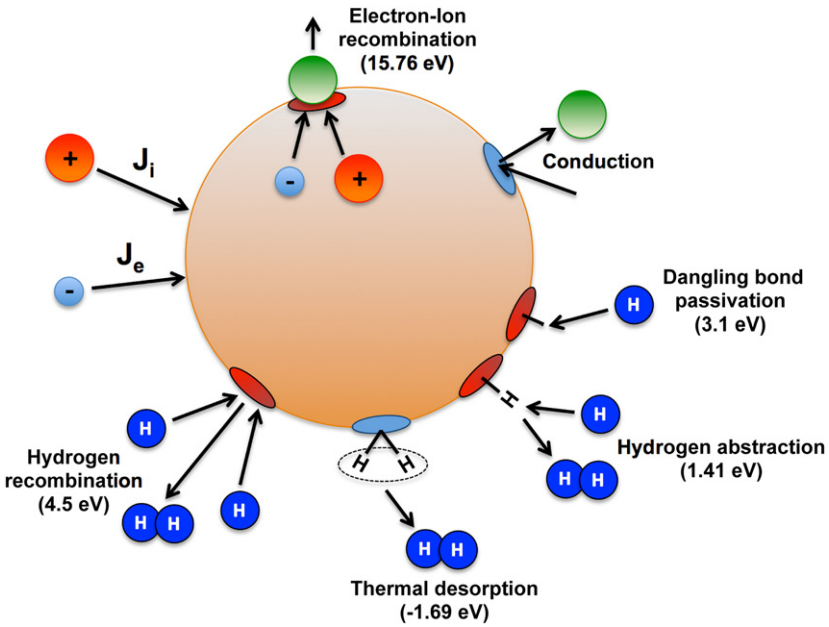

Figure 2. Heating and cooling events occurring on the silicon nanoparticle surface. Heating events are indicated with red dots on the nanoparticle surface while cooling events are shown as blue dots. The electron–ion recombination energy is equal to the argon ionization potential of 15.76 eV. Dangling bond passivation, hydrogen abstraction and hydrogen recombination deliver 3.1 eV, 1.41 eV and 4.5 eV, respectively. Cooling occurs mainly through collisions with colder gas atoms. At 900 K and higher, thermal desorption of hydrogen starts to play a role, where the energy loss is equal to 1.69 eV for each desorbed hydrogen molecule.

2.4. Nanoparticle heating model

The nanoparticle temperature (T_p) was calculated from the transient particle energy balance,

$$\frac{4}{3}\pi r^3 \rho C \frac{dT_p}{dt} = G - L, \quad (1)$$

where ρ is the silicon mass density, C is the heat capacity, G is the heating term and L is the cooling term as previously described in [24]. Briefly, particles are heated through electron–ion recombination at their surface and through reactions involving hydrogen atoms, as shown in figure 2. The main loss is due to conduction to the background gas, which we assume is argon. As the gas density is significantly higher than the ion density and hydrogen density, we consider this loss term as a continuous process. Radiative cooling is negligible compared to conductive cooling because the nanoparticle diameter is smaller than the emitted wavelength [30].

As described in [24], equation (1) is solved by discretizing the expression using a typical time step of 10^{-10} s. Initially the temperature of the nanoparticle is equal to the gas temperature, and the particle does not have any charge or hydrogen on its surface. A Monte Carlo approach is applied to select either an ion or electron to collide with the nanoparticle [31]. The hydrogen reactions occurring at the nanoparticle surface are evaluated from a separate secondary loop. The model keeps track of the charge, temperature, and hydrogen coverage of the nanoparticle at each time step. These quantities determine the probability of electron–ion recombination and hydrogen reactions. The input parameters such as the ion density, electron temperature and hydrogen density are obtained from the plasma diagnostics, as described in section 2.3. Equilibrium conditions are reached after less than a millisecond. Further details are described in [24].

3. Results and discussion

3.1. Nanoparticle characterization

We synthesized amorphous nanoparticles under identical conditions in the first plasma and injected them into the second plasma. We then studied whether these amorphous nanoparticles are crystallized under different plasma powers in the second plasma to study their crystallization. The nanoparticle size was varied by adjusting the argon flow rate, and experiments were conducted for 3, 4 and 5 nm nanoparticles. Figures 1(*b*) and (*c*) show the XRD and Raman spectra from 4 nm nanoparticles as a function of power used to maintain the second plasma. The XRD and Raman spectra for 3 and 5 nm nanoparticles are presented in the online supplemental section (stacks.iop.org/JPhysD/47/075202/mmedia). The XRD patterns clearly show an increase in silicon nanoparticle crystallinity as the secondary plasma power is increased. Raman scattering confirms this trend. In figure 1(*b*), the Raman scattering peak at 520 cm^{-1} originates from crystalline silicon, whereas the broad peak around 480 cm^{-1} is typically observed from amorphous silicon. These data also confirm that nanoparticles produced in the first plasma are amorphous, because there are no crystalline peaks in the XRD or the Raman spectra when the second plasma is not turned on (0 W).

Figures 1(*b*) and (*c*) show that above a threshold power the nanoparticles exiting the second plasma are completely crystallized. For 3 nm nanoparticles, this threshold power is 20 W; both Raman spectra and XRD show fully developed crystalline peaks at this power. The crystallization threshold power increases to 30 W and 40 W for 4 nm and 5 nm nanoparticles, respectively. The nanoparticle size and crystallinity were also characterized using TEM. For

example, the bright-field images in figures 1(*d*) and (*e*) show the transformation of 5 nm amorphous nanoparticles to nanocrystals. TEM images also show that the nanoparticle size does not increase significantly upon crystallization. This indicates that the nanoparticles do not coalesce or continue to grow in the second plasma. In summary, the TEM, XRD and Raman spectroscopy studies are consistent and confirm the existence of a threshold power required for crystallization.

3.2. Plasma properties

We measured the electron temperature (T_e), the ion density (n_i), and the hydrogen density (n_H) as a function of power used to maintain the second plasma and determined the respective values of these properties needed to crystallize the amorphous nanoparticles made in the first plasma. These values were used as inputs to our model for determining the nanoparticle temperature as a function of time during the transit through the second plasma.

Figure 3(*a*) shows the ion densities as a function of second plasma power for the primary plasma conditions used to produce the three different nanoparticle sizes. Hereafter and in all figures, these plasma conditions will be referred to with the size of the nanoparticles they produce. As expected, the ion density increases with increasing plasma power. The ion density increases faster with increasing power for plasma conditions under which smaller nanoparticles are synthesized. This is caused by the difference in argon flow rates. This change in argon flow rate is used to synthesize the different sized nanoparticles while maintaining a constant pressure. To decrease the nanoparticle size, the argon flow rate is increased which in turn increases the argon/silane ratio, reduces the partial pressure of silane, and decreases the nanoparticle residence time in the plasma. The resulting change in the gas composition affects the ion density and variation with plasma power.

Figures 3(*b*) and (*c*) show the electron temperature and the hydrogen atom density as a function of the secondary plasma power for the three different primary plasma conditions that yield 3, 4 and 5 nm silicon nanoparticles. The electron temperature found for the conditions under which 5 nm particles are produced is significantly higher compared to the others. This increase in electron temperature could be caused by the reduced argon partial pressure. As the silane is diluted in helium, the partial pressure of helium will be highest for 5 nm nanoparticles, causing an increase in electron temperature. The slight decrease in electron temperature for increasing powers can be explained by higher ion and electron densities at higher powers, leading to a lowering of the electron temperature.

The hydrogen density is also a strong function of the secondary plasma power and the primary plasma conditions used for making different size nanoparticles. For example, the hydrogen density is the largest under the conditions used for making 5 nm nanoparticles because the silane-to-argon ratio and, consequently, the silane partial pressure are the highest. Increasing the argon flow rate dilutes the silane and the hydrogen density decreases.

The gas temperature in the plasma was measured by placing a thermocouple directly into the secondary plasma.

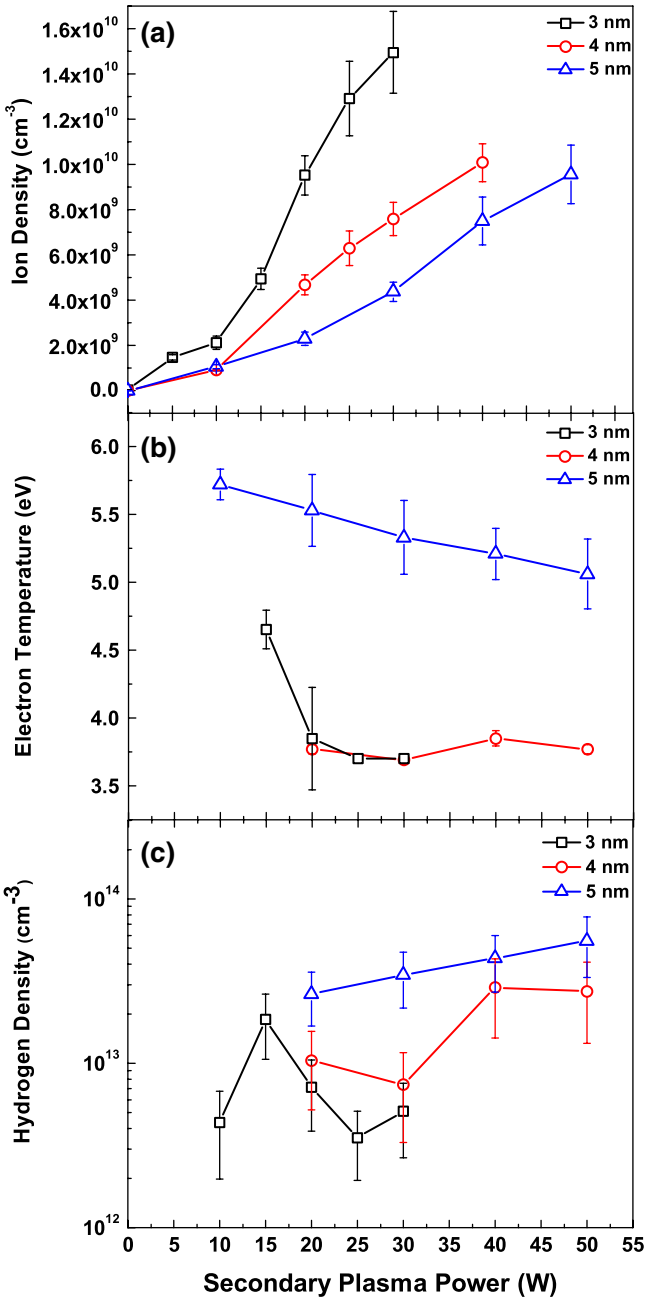

Figure 3. (*a*) Ion density, (*b*) electron temperature and (*c*) hydrogen density in the second plasma as a function of the secondary plasma power for several different conditions used to operate the primary plasma. The primary plasma conditions are referred to with the size of the nanoparticles they produce (see table 1).

To measure the temperature the plasma was switched off briefly. The temperature values ranged from 370 K up to 430 K, depending on the applied power to the plasma. This agrees with typical gas temperatures that are found in nonthermal plasmas [1].

3.3. Nanoparticle heating model

The electron temperature, ion density and hydrogen density were used as inputs to the nanoparticle heating model. Figure 4 shows the calculated nanoparticle temperature as a function

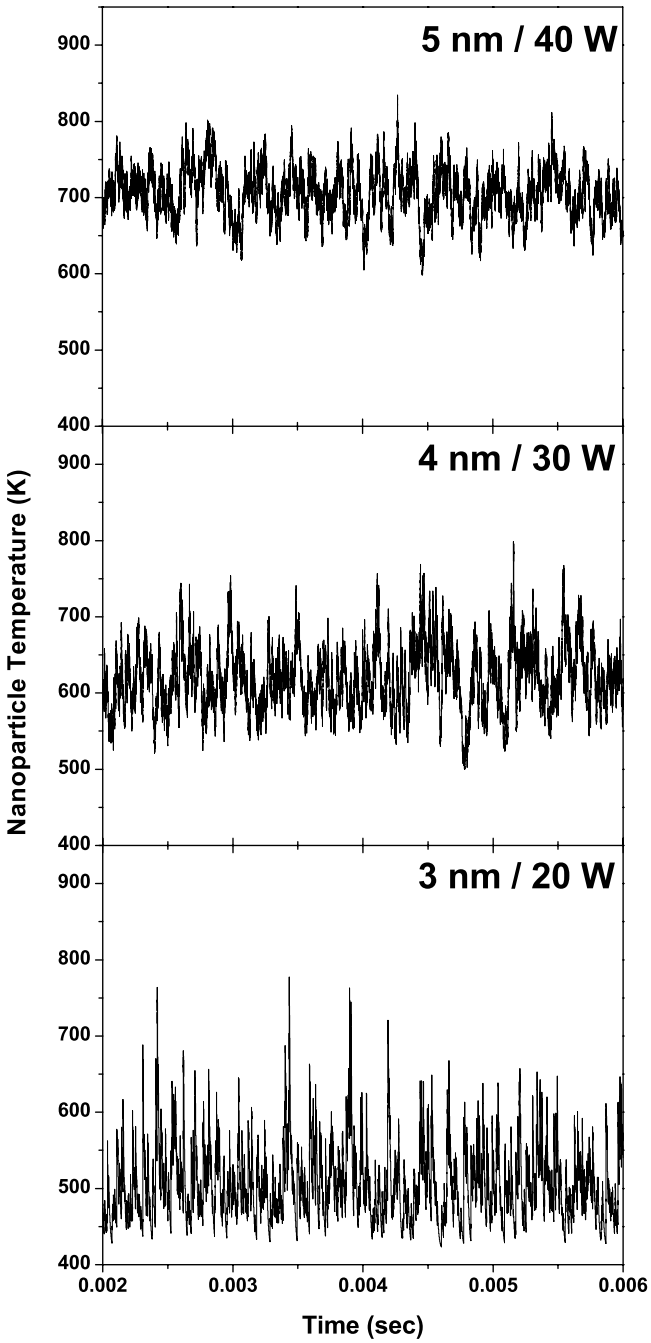

Figure 4. Time-dependence of nanoparticle temperature calculated from the transient energy balance. The temperatures of each nanoparticle with different size are evaluated at the critical power where the nanoparticles begin to crystallize. This critical power was determined from XRD and Raman scattering data. The nanoparticles in the size range of 3–5 nm can reach temperatures significantly above the gas temperature.

of the three nanoparticle sizes. While the gas temperature is only 400 K, the nanoparticles reach much higher temperatures, sufficient to crystallize the amorphous nanoparticles injected from the primary plasma. The 3 nm particles show more frequent and much larger temperature fluctuations than the 5 nm particles because of their smaller mass. While the average temperature of these 3 nm particles is close to the gas temperature, the fluctuations are large enough to raise their instantaneous temperature to as high as 700 K. Conduction to the background gas causes the rapid cooling after every heating event. The temperature exponentially decays within microseconds after every heating event occurs.

Raman spectra show that a large fraction of the nanoparticles are still amorphous, even at the threshold plasma power for all three sizes. While the average nanoparticle temperature is sufficient for crystallization, there will be a distribution in both the temperature as well as the size of the nanoparticles. Thus, some fraction of the nanoparticles will still remain below the critical crystallization temperature, while a large portion reach the temperatures required for crystallization. When the power is increased further, more of the nanoparticles reach temperatures higher than the crystallization temperature and the fraction of nanocrystals increases.

Comparison of the 4 nm nanoparticle temperature presented in figure 4 with XRD and Raman spectra suggests that the critical crystallization temperature is between 600 and 700 K for 4 nm nanoparticles. This is reached when the secondary plasma power is at or above 30 W. Figure 5 shows the calculated nanoparticle temperatures for powers below and above this threshold power. Indeed, figure 5 shows that, at 20 W, the average nanoparticle temperature decreases to approximately 550 K, well below the temperature required for crystallization. However, at higher plasma powers (40 W) the nanoparticle temperature increases to 750 K. This agrees with the trend seen from *ex-situ* nanoparticle analysis, where the nanoparticles remained amorphous for low plasma powers, indicating insufficient nanoparticle heating. This supports the hypothesis that nanoparticle heating is the mechanism for nanoparticle crystallization.

Figure 4 also shows that the average nanoparticle temperature increases with increasing size. This increase is due to the increase in the hydrogen density and the electron temperature, as shown in figure 3. As the nanoparticle mass increases, the individual stochastic recombination events and reactions that release energy do not cause significant temperature spikes anymore. However, higher electron temperature and larger hydrogen densities increase the heating rate for 5 nm particles. This increase is despite decreasing ion densities. Thus the 5 nm particles can still reach temperatures that are sufficiently high for crystallization.

The relative importance of heating due to electron–ion recombination and heating due to reactions of radicals on the nanoparticle surface is shown in figure 6 for 3 nm and 5 nm nanoparticles. For 3 nm nanoparticles, the electron–ion recombination events and hydrogen reactions both contribute about equally to the nanoparticle heating, leading to nanoparticle temperatures well above the gas temperature. When time-averaged heating contributions are calculated, the contribution of electron–ion recombination is 43% while hydrogen reactions contribute 57% of the total nanoparticle heating. However, the temperature spikes are the result of the more energetic electron–ion recombination events and enable the nanoparticles to reach temperatures of up to 700 K.

The dominant heating mechanism for 5 nm nanoparticles is different. The heating due to electron–ion recombination

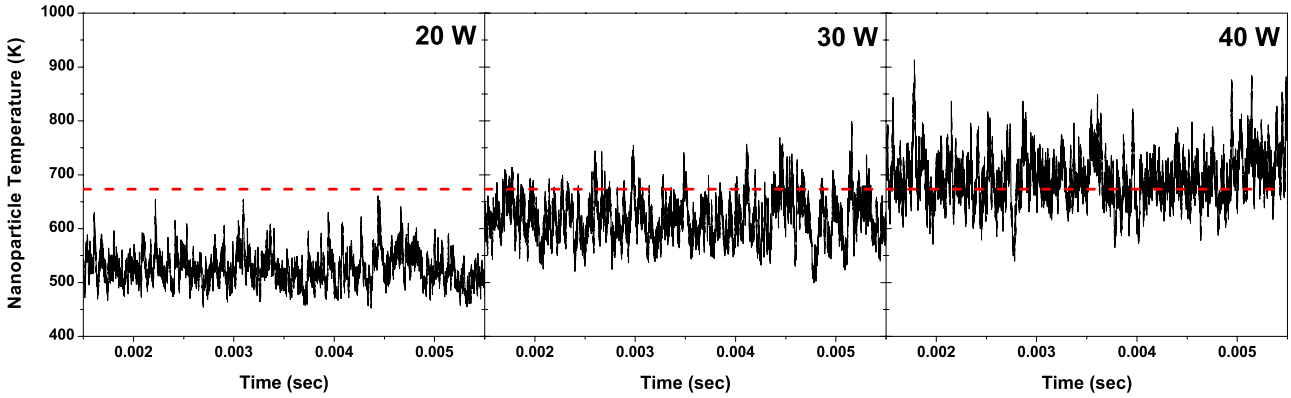

Figure 5. The temperature of a 4 nm silicon nanoparticle for three different secondary plasma powers. The temperature required for nanoparticle crystallization from [19] is indicated by the dashed line. The average nanoparticle temperature increases with increasing plasma powers and exceeds the crystallization temperature once the power is equal to or larger than 30 W.

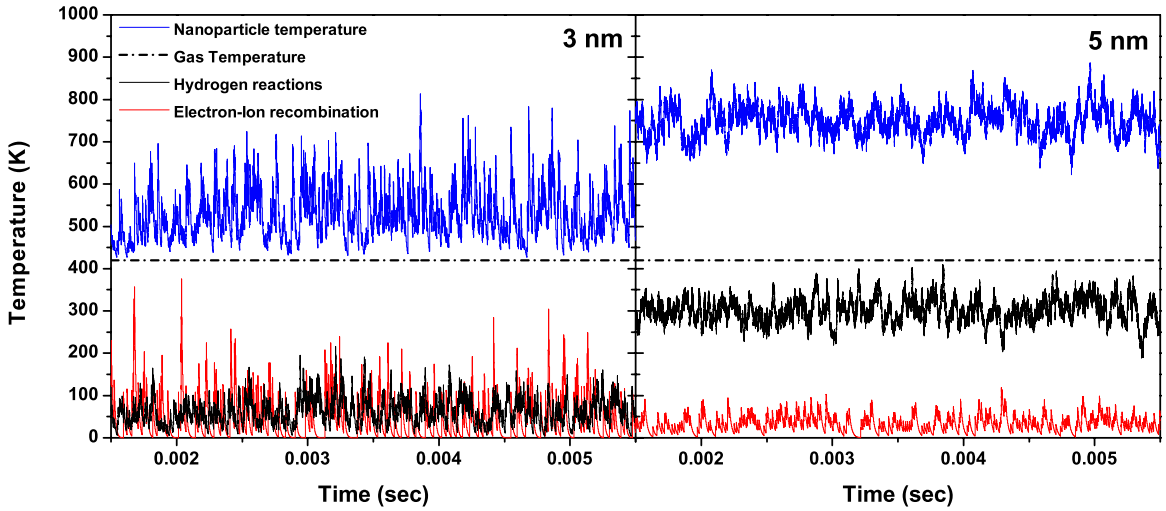

Figure 6. Relative contributions of electron–ion recombination and hydrogen reactions to nanoparticle heating for 3 and 5 nm nanoparticles. For 3 nm nanoparticles, both electron–ion recombination and hydrogen reactions equally contribute to nanoparticle heating. For 5 nm nanoparticles hydrogen reactions dominate nanoparticle heating.

is reduced significantly, caused by the increase in mass of the nanoparticle and the lower ion density. The dominant nanoparticle heating mechanism is hydrogen atom reactions on the nanoparticle surface because the hydrogen density is higher under the conditions used for synthesizing the 5 nm nanoparticles. This is the case even though the energy released for each reaction is far lower than the electron–ion recombination reactions. Integration shows that for these plasma conditions, hydrogen reactions deliver 90% of the energy to heat the particle to the crystallization temperature.

4. Conclusion

Here we studied the crystallization mechanism during nonthermal plasma synthesis of silicon nanoparticles. We decoupled the nanoparticle synthesis from nanoparticle heating by separating them into two separate plasma regions using a tandem plasma configuration. Using this approach, we were able to determine the electron temperature, ion density and hydrogen density required for complete crystallization of silicon nanoparticles with various sizes, and determine the physical processes that lead to nanoparticle heating. As the nanoparticles become larger, the plasma power required for crystallization increases. From *ex-situ* nanoparticle characterization we found that the critical threshold powers were 20 W, 30 W and 40 W for nanoparticle sizes of 3 nm, 4 nm and 5 nm, respectively.

The electron temperature, ion density and hydrogen density in the secondary plasma were measured using ion-flux probe and optical emission spectroscopy. Using these measured plasma properties the nanoparticle temperature is calculated by integrating the nanoparticle energy balance. It was found that the nanoparticle temperature is significantly higher than the gas temperature. For plasma conditions at which the nanoparticles become crystalline, the nanoparticles reach temperatures which are sufficient for crystallization, confirming that the nanoparticles crystallize due to heating in the plasma. For the smaller 3 nm nanoparticles, both electron–ion recombination and hydrogen reactions contribute to the increase in nanoparticle temperature. However, for 5 nm particles the main contribution to nanoparticle heating are the reactions of hydrogen atoms on the nanoparticle surface. This

study allowed us to determine the necessary plasma conditions for the formation of crystalline silicon nanoparticles, and gave valuable insight into the physical origin of nanoparticle crystallization. While we focused on silicon nanoparticles, the approach used in this article is applicable to other materials as well. Thus, this method can promote a better understanding of the general processes of particle crystallization in plasmas and could even be used to predict the viability of achieving crystalline nanoparticles of new materials via a nonthermal plasma synthesis.

Acknowledgments

This work was supported in part by the DOE Plasma Science Center for Predictive Control of Plasma Kinetics. Partial support by the NSF/DOE Partnership in Basic Plasma Science through grants DOE/DE- SC0002391 and NSF CBET-0903842 is acknowledged, which provided support for NK, MM and URK. Parts of this work were carried out in the Characterization Facility, University of Minnesota, which receives partial support from NSF through the MRSEC program.

References

[1] Mangolini L, Thimsen E and Kortshagen U 2005 High-yield plasma synthesis of luminescent silicon nanocrystals *Nano Lett.* **5** 655–9

[2] Pi X D, Liptak R W, Deneen Nowak J, Wells N P, Carter C B, Campbell S A and Kortshagen U 2008 Air-stable full-visible-spectrum emission from silicon nanocrystals synthesized by an all-gas-phase plasma approach *Nanotechnology* **19** 245603

[3] Kortshagen U R 2009 Nonthermal plasma synthesis of semiconductor nanocrystals *J. Phys. D.: Appl. Phys.* **42** 113001

[4] Bapat A, Gatti M, Ding Y, Campbell S A and Kortshagen U R 2007 A plasma process for the synthesis of cubic-shaped silicon nanocrystals for nanoelectronic devices *J. Phys. D: Appl. Phys.* **40** 2247–57

[5] Holman Z C and Kortshagen U R 2010 A flexible method for depositing dense nanocrystal thin films: impaction of germanium nanocrystals *Nanotechnology* **21** 335302

[6] Gresback R, Nozaki T and Okazaki K 2011 Synthesis and oxidation of luminescent silicon nanocrystals from silicon tetrachloride by very high frequency nonthermal plasma *Nanotechnology* **22** 305605

[7] Gresback R, Hue R, Gladfelter W L and Kortshagen U R 2011 Combined plasma gas-phase synthesis and colloidal processing of InP/ZnS core/shell nanocrystals *Nanoscale Res. Lett.* **6** 68

[8] Lieberman M A and Lichtenberg A J 1994 *Principles of Plasma Discharges and Materials Processing* (New York: Wiley)

[9] Goree J 1999 Charging of particles in a plasma *Plasma Sources Sci. Technol.* **3** 400–6

[10] Matsoukas T and Russell M 1995 Particle charging in low-pressure plasmas *J. Appl. Phys.* **77** 4285–92

[11] Galli F and Kortshagen U R 2010 Charging, coagulation, and heating model of nanoparticles in a low-pressure plasma accounting for ion–neutral collisions *IEEE Trans. Plasma Sci.* **38** 803–9

[12] Schweigert V A and Schweigert I V 1996 Coagulation in a low-temperature plasma *J. Phys. D: Appl. Phys.* **29** 655–9

[13] Kortshagen U and Bhandarkar U 1999 Modeling of particulate coagulation in low pressure plasmas *Phys. Rev.* E **60** 887–98

[14] Selwyn G S 1993 Trapping and behavior of particulates in a radio frequency magnetron plasma etching tool *J. Vac. Sci. Technol.* A **11** 1132

[15] Anthony R J and Kortshagen U R 2009 Photoluminescence quantum yields of amorphous and crystalline silicon nanoparticles *Phys. Rev.* B **80** 115407

[16] Rowe D J, Jeong J S, Mkhoyan K A and Kortshagen U R 2013 Phosphorus-doped silicon nanocrystals exhibiting mid-infrared localized surface plasmon resonance *Nano Lett.* **13** 1317–22

[17] Erwin S C, Zu L, Haftel M I, Efros A L, Kennedy T A and Norris D J 2005 Doping semiconductor nanocrystals *Nature* **436** 91–4

[18] Goldstein A N 1996 The melting of silicon nanocrystals: submicron thin-film structures derived from nanocrystal precursors *Appl. Phys.* A **62** 33–7

[19] Hirasawa M, Orii T and Seto T 2006 Size-dependent crystallization of Si nanoparticles *Appl. Phys. Lett.* **88** 093119

[20] Roura P, Farjas J, Pinyol A and Bertran E 2007 The crystallization temperature of silicon nanoparticles *Nanotechnology* **18** 175705

[21] Daugherty J E and Graves D B 1993 Particulate temperature in radio frequency glow discharges *J. Vacuum Sci. Technol.* A **11** 1126

[22] Swinkels G H P M, Kersten H, Deutsch H and Kroesen G M W 2000 Microcalorimetry of dust particles in a radio-frequency plasma *J. Appl. Phys.* **88** 1747–55

[23] Stoffels E, Stoffels W W, Kersten H, Swinkels G H P M and Kroesen G M W 2001 Surface processes of dust particles in low pressure plasmas *Physica Scripta* **T89** 168

[24] Mangolini L and Kortshagen U R 2009 Selective nanoparticle heating: another form of nonequilibrium in dusty plasmas *Phys. Rev.* E **79** 026405

[25] Maurer H R and Kersten H 2011 On the heating of nano- and microparticles in process plasmas *J. Phys. D: Appl. Phys.* **44** 174029

[26] Hawa T and Zachariah M 2005 Coalescence kinetics of bare and hydrogen-coated silicon nanoparticles: A molecular dynamics study *Phys. Rev.* B **71** 165434

[27] Braithwaite N St J, Booth J-P and Cunge G 1996 A novel electrostatic probe method for ion flux measurements *Plasma Sources Sci. Technol.* **5** 667–84

[28] Petcu M C, Bronneberg A C, Sarkar A, Blauw M A, Creatore M and van de Sanden M C M 2008 A capacitive probe with shaped probe bias for ion flux measurements in depositing plasmas *Rev. Sci. Instrum.* **79** 115104

[29] Malyshev M and Donnelly V 1999 Trace rare gases optical emission spectroscopy: nonintrusive method for measuring electron temperatures in low-pressure, low-temperature plasmas *Phys. Rev.* E **60** 6016–29

[30] Maurer H R, Basner R and Kersten H 2010 Temperature of particulates in low-pressure rf-plasmas in Ar, Ar/H2 and Ar/N2 mixtures *Contrib. Plasma Phys.* **50** 954–61

[31] Goree J and Cui C 1994 Fluctuations of the charge on a dust grain in a plasma *IEEE Trans. Plasma Sci.* **22** 151–8